

Research papers

Capacity and degradation mode estimation for lithium-ion batteries based on partial charging curves at different current rates

Julius Schmitt ^{a,*}, Mathias Rehm ^a, Alexander Karger ^{a,b}, Andreas Jossen ^a

^a Technical University of Munich, School of Engineering and Design, Department of Energy and Process Engineering, Chair of Electrical Energy Storage Technology, Arcisstraße 21, 80333 Munich, Germany

^b TWAICE Technologies GmbH, Joseph-Dollinger-Bogen 26, 80807 Munich, Germany



ARTICLE INFO

Dataset link: <https://mediatum.ub.tum.de/1690455>

Keywords:

Lithium-ion battery
State of health estimation
Degradation modes
OCV curve
Capacity estimation
Partial charging

ABSTRACT

The open circuit voltage (OCV) curve of a lithium-ion cell can be described as the difference between the half-cell open circuit potential curves of both electrodes. Fitting a reconstructed OCV curve to the OCV curve of an aged cell allows identification of degradation modes. In this study, we show that this method can also be applied to partial charging curves of a commercial cell with silicon-graphite and NMC-811 as electrode materials. Both the degradation modes and the remaining cell capacity can be determined from the reconstructed OCV curve. For the investigated cell, accurate OCV reconstruction and degradation mode estimation can be obtained from C/30 partial charging curves if the state of charge (SOC) window between 20 % and 70 % is available. We show that the method is also applicable to charging curves at higher current rates if the additional overpotential is considered by subtracting a constant voltage offset. Capacity estimation with an accuracy of 2 % of the nominal capacity is possible for current rates up to approximately C/4 if partial charging curves between 10 % and 80 % SOC are used, while a maximum current rate of C/15 should be used for accurate estimation of the degradation modes.

1. Introduction

One of the most important functions of a battery management system (BMS) for lithium-ion batteries is monitoring the remaining capacity of the battery over its lifetime in order to provide accurate estimates of the available energy and power. The fraction of the initial capacity that is still usable is often referred to as the state of health (SOH). The methods for SOH estimation for lithium-ion batteries that have been proposed in the literature can be categorized into three main categories:

1. Electrical model-based: the electrical behavior of the battery is described by a model. The model parameters are updated during aging by minimizing the difference between an estimated and measured model output, which is usually the terminal voltage. The obtained model parameters either directly include the SOH or indirectly allow its calculation [1–9].
2. Feature correlation-based: the correlation between a measurable feature and the SOH is established via lab experiments. In the application, the correlation is then used to calculate the SOH whenever it is possible to measure the feature [10–21].

3. Aging model-based: a pre-parameterized empirical aging model is used to calculate the SOH based on the operation history of a battery [22,23].

The main drawback of feature correlation-based and aging model-based methods is the necessity for tedious and costly aging studies for model parametrization. This is avoided by electrical model-based methods that do not require aging experiments during algorithm development except for validation purposes and can therefore be implemented more quickly with less effort.

One of the major challenges for electrical model-based SOH estimation is the change in the shape of the open circuit voltage (OCV) curve, i.e., the relationship between state of charge (SOC) and the OCV, during aging. Neglecting these changes leads to a significant decrease in the accuracy of electrical models during aging [24,25] so that methods to update the OCV curve are therefore needed [1]. The most commonly used framework to describe the OCV curve during aging is the mechanistic modeling approach introduced by Dubarry et al. [24] which has been used by many authors over the last decade [5,7,8,26–36]. In this framework, the OCV curve is modeled as the difference between the open circuit potential (OCP) curves of the cathode and

* Corresponding author.

E-mail address: julius.schmitt@tum.de (J. Schmitt).

the anode. Changes in the OCV curve are traced back to degradation modes, which are clusters of degradation mechanisms occurring at the cell components. The most important degradation modes are the loss of active material at the anode (LAM_{an}), the loss of active material at the cathode (LAM_{cat}) and the loss of lithium inventory (LLI) [24]. In many studies, additional degradation modes such as resistance increase [5,24], increase in inhomogeneity [30], and component specific degradation of silicon in silicon-graphite blend electrodes [33] are also considered. The degradation modes are usually quantified by fitting reconstructed OCV curves to low-current charging or discharging curves.

This framework can be used to develop algorithms for SOH estimation that take changes in the OCV curve into account [2,3,7,8,37], and which can be included in the class of electrical model-based methods. In this study, we present such an algorithm for both SOH and degradation mode estimation and systematically evaluate its performance when applied to partial charging curves and charging curves at higher current rates. These aspects are highly important for the practical applicability of the algorithm because batteries are usually only partially charged and/or charged at higher currents in applications.

There are some papers that report on the reconstruction of OCV curves based on partial cycles: Yang et al. applied degradation mode analysis to partial charging curves at a current rate of C/3 [37]. They reported that the method performs well for both capacity estimation and degradation mode analysis at this current rate, if the charging curves at least include the range between 20–70% SOC. Lee et al. studied the theoretical estimation uncertainty of electrode-alignment parameters based on partial OCV curves using Cramér-Rao bounds [8]. They found that the analytical error bound of alignment parameters decreases with increasing size of the SOC window used for the curve alignment and that the inclusion of regions with a high voltage slope is beneficial for an accurate alignment parameter estimation. Marongiu et al. reported that accurate capacity estimation for a LFP/graphite cell is possible if the length of the upper two full-cell OCV plateaus is observable [2,3].

Methods for OCV reconstruction and degradation mode estimation based on constant current phases at higher current rates have also been investigated: Chen et al. showed that the degradation modes can be determined from full and partial constant current (CC) discharging curves at 0.3C using incremental capacity (IC) and differential voltage (DV) peak tracking [38]. In the work by Yang et al. the overpotential at higher current rates is compensated by adding an ohmic resistance term to the model used for calculating the terminal voltage and by using the weighted sum of the mean square deviation of both OCV and DV as a cost function for the OCV reconstruction [37]. Lu et al. investigated compensating the overpotential during charging/discharging measurements by adding a linearly SOC-dependent resistance term but did not achieve accurate results for OCV reconstruction using this approach [34]. Instead, they recommended using the lowest possible current rate for OCV and OCP measurements. Apart from this, there are papers in which partial charging curves or charging curves at higher current rates were used to directly estimate the remaining cell capacity via feature-correlation based methods for which a pre-parametrized model is needed [13,18,20,21,39,40].

In the scope of this work, an algorithm for SOH estimation and degradation mode estimation based on OCV reconstruction is presented and its accuracy is systematically evaluated for partial charging curves comprising different SOC ranges and for charging curves at different current rates. To the best of our knowledge, a systematic evaluation of the impact of the SOC range and the current rate of charging curves used as input data for OCV reconstruction has yet to be presented in the literature. We concentrate on CC charging curves as input as this type of data can be regularly measured in many applications. The algorithm could be applied to the analysis of field data or implemented in a BMS for on-board battery monitoring. No parametrization of an aging model or correlation of a feature with SOH is necessary. The

algorithm is independent of SOC estimation and the updated OCV curve, which is obtained as an additional output, can be used for other BMS tasks that depend on an accurate OCV curve such as model-based SOC estimation [1,2,6,25,41].

2. Experimental

2.1. Overview

Commercially available cells of the type INR18650-MJ1 made by LG Chem were investigated in this study. The 18650 format cells have a nominal minimum capacity (C_{nom}) of 3.35 Ah. C-rates used in this study refer to this capacity. The anode active material of the cells is a blend of silicon-based compounds and graphite. Different values for the mass ratio of silicon in the anode material within the range of 1 wt.% to 5 wt.% have been reported for this cell type [33,42–45]. The cathode active material is NMC-811 [43,44]. One equivalent full cycle (EFC) is defined as the charge throughput of twice the nominal capacity, which is 6.7 Ah. Whenever a constant voltage (CV) phase was applied, the cut-off current was 50 mA.

An overview of the conducted experiments is given in Fig. 1(a). The cells were operated at 25 °C ambient temperature inside a temperature chamber using a CTS battery test system from BaSyTec. An aging test sequence consisting of a capacity test, a pulse test, an application phase, a charging rate test and a continuous cycling phase was repeatedly applied to ten cells of the aforementioned type. This aging test sequence was applied up to 26 times with a total duration (t_{tot}) of 486 days or until a temperature of 60 °C (T_{max}) at the cell surface was exceeded at any point during the tests. After completion of the last iteration of the aging test sequence, another capacity test and pulse test were performed. 158 days after the aging test sequence was stopped, an extended charging rate test was conducted with some of the cells. Details on the aging test sequence and the extended charging rate test are presented below. An overview on the experimental procedures applied to the individual cells is provided in Table A.1 in the appendix. The experimental data measured in the scope of this study is made available in [46].

2.2. Aging test sequence

Capacity test. The cells were cycled two times using constant current constant voltage (CCCV) charging at a current rate of C/2 to 4.2 V and CCCV discharging with a current rate of C/5 to 2.5 V. The charge extracted during the CC part of the second discharging is denoted as $C_{C/5\text{ dch}}$.

Pulse test. The cells were charged to 50% SOC and current pulses with a duration of 10 s and with current rates of C/3, 2C/3 and 1C were applied in both the discharging and charging directions. There was a relaxation period of 30 min after setting the SOC and a 10 min relaxation period between the pulses.

Application phase. The application phase was designed to simulate the conditions in a battery electric vehicle. It contains dynamic operation with a profile based on the worldwide harmonized light vehicles test procedure (WLTP), CCCV charging procedures and rest times with several hours of duration. The vehicle model presented in [47] was used to convert the WLTP velocity profile to power requirements. The application phase has a total duration of three days. The measurement data recorded during the application phases is not further discussed within this work but might be used in future studies. We publish the measurement data recorded during the application phases at different aging states in [46]. Additional information on the application phase and the vehicle model is provided in Appendix B.

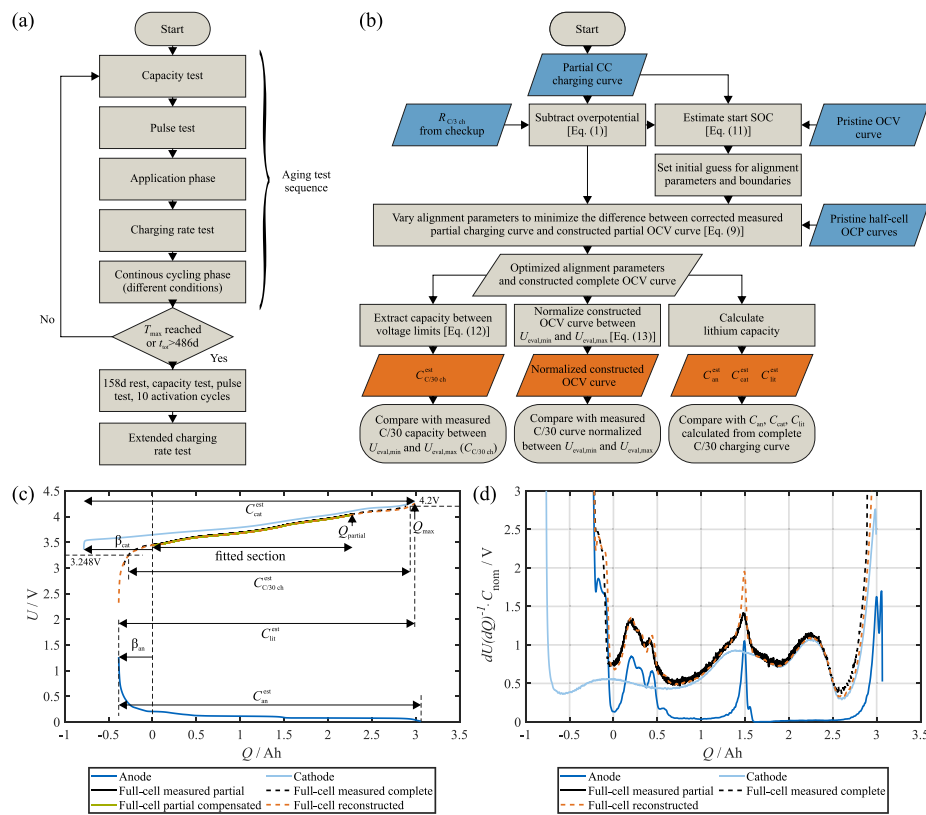


Fig. 1. (a) Flowchart describing the experimental procedure. (b) Flowchart describing the algorithm for capacity estimation, OCV reconstruction and degradation mode analysis based on partial charging curves. Inputs are highlighted in blue, outputs are highlighted in orange. (c) Example for fitting half-cell OCP curves to a partial charging curve (10–80% SOC) with compensation of the overpotential. A C/10 charging process is shown for a new cell and the X-axis indicates charge throughput with respect to the starting point of the partial curve used for the fitting. (d) Differential voltage of the curves shown in (c). (For interpretation of the references to color in this figure legend, the reader is referred to the web version of this article.)

Charging rate test. The cells were repeatedly CC-discharged to 2.5 V with a current rate of C/5 and then charged to 4.2 V using different rates. The procedure was executed using CCCV charging at 1 C, C/2 and 0.264 C and for constant power constant voltage (CPCV) charging at 3.183 W. Finally, the cells were CC discharged to 2.5 V at a current rate of C/5 and, after a relaxation period lasting 6 h, the cells were CC charged at a rate of C/30 until they reached a terminal voltage of 4.2 V. After another 6 h relaxation period, the cells were CC-discharged at a rate of C/30 until they reached a terminal voltage of 2.5 V.

The power of 3.183 W corresponds to the power at which each cell of a hypothetical battery pack consisting of 3456 cells (96s36p configuration, total nominal energy of 42 kWh) would be charged, if the total charging power was 11 kW, a value which is typical of home-installed AC charging stations. 0.264 C is the current rate corresponding to this power at the nominal cell voltage.

Continuous cycling phase. Two of the cells were kept under open circuit conditions for eight days after being CC charged at C/2 to 3.7 V. The remaining eight cells were continuously cycled for eight days under different conditions. Four sets of cycling conditions were used and two of the cells were cycled under each set of conditions. All of the cells were CCCV-charged at a rate of C/2. Different voltage limits and discharging procedures were used. They are listed in Table 1 along with the labels that are used to refer to the respective cells below. The cells labeled WLTP were discharged using the same dynamic discharging profile that was used in the application phase. The cells that were kept under open circuit conditions during this phase are denoted as “Only checkups” as they were only operated during the capacity, pulse and charging rate tests as well as the application phases but otherwise were only subject to calendar aging.

Table 1
Operation conditions applied during the continuous cycling phase.

Label	U_{min}	U_{max}	Discharge procedure
2.5 V-4.2 V	2.5 V	4.2 V	1 C CC
2.5 V-4.0 V	2.5 V	4.0 V	1 C CC
3.6 V-4.2 V	3.6 V	4.2 V	1 C CC
WLTP	2.5 V	4.2 V	WLTP profile

2.3. Extended charging rate test

Prior to the actual extended charging rate test, a capacity and a pulse test, ten activation cycles (1 C CC discharging to 2.5 V, C/2 CCCV charging to 4.2 V) and then another capacity and pulse test were applied. During the extended charging rate test, the cells were CCCV charged to 4.2 V using different current rates. The current rates during the charging phases were 0.264 C, C/6, C/8, C/10, C/12, C/15, C/20, C/25 and C/30. Between the charging phases, the cells were consistently CC discharged to 2.5 V at a current rate of C/5 with a subsequent 6 h relaxation phase. The extended charging rate test was conducted with the cells that had been aged under the conditions “3.6 V-4.2 V” and “Only checkups” as well as with two cells that had not been cycled before.

3. Algorithm and validation method

The algorithm for SOH and degradation mode estimation presented in this study is based on the mechanistic modeling framework introduced by Dubarry et al. [24]. The main aim of this study is to systematically evaluate its estimation accuracy for partial charging

curves and for charging curves at higher current rates. Therefore, the algorithm is implemented in such a way that it can be applied not only to complete charging curves, as is usually the case for degradation mode analysis, but also to partial charging curves without prior knowledge of the start and end SOC.

A flow chart representing the working principle of the algorithm is shown in Fig. 1(b). The main idea is to reconstruct the complete OCV curve based on a partial OCV curve. The cell capacity can then be estimated as the part of the reconstructed OCV curve that lies between the upper and lower cut-off voltage. In this study, we consider the charging curve at C/30 to be the reference for the OCV curve [38]. For those cases where charging curves at higher current rates are analyzed, an estimate for the additional overpotential in comparison to the C/30 charging curve is subtracted from the voltage data. The compensated partial charging curve $U_{\text{OCV}}(Q)$ as a function of the charge throughput measured during the partial charging Q is calculated according to

$$U_{\text{OCV}}(Q) = U_{\text{meas}}(Q) - (I - I_{\text{C}/30}) \cdot R_{\text{C}/3 \text{ ch}} \quad (1)$$

where $U_{\text{meas}}(Q)$ is the measured terminal voltage, I is the charging current, $I_{\text{C}/30}$ is the current applied during C/30 charging and $R_{\text{C}/3 \text{ ch}}$ is the resistance that is calculated from the C/3, 10 s charging pulse at 50% SOC during the pulse test preceding the respective charging rate test. $R_{\text{C}/3 \text{ ch}}$ is calculated as

$$R_{\text{C}/3 \text{ ch}} = \frac{\Delta U}{\Delta I} \quad (2)$$

where ΔU is the difference between the voltage measured at the end of the pulse and the voltage measured directly before the pulse. ΔI is the current amplitude of the pulse.

For the reconstruction of the full-cell OCV curve, the normalized pristine half-cell OCP curves which are functions of the electrode SOC

$$U_{\text{cat}} = f_{\text{cat}}(\text{SOC}_{\text{cat}}) \quad (3)$$

$$U_{\text{an}} = f_{\text{an}}(\text{SOC}_{\text{an}}) \quad (4)$$

need to be transformed into the coordinate system (Q) of the partial full-cell curve by linear scaling with the estimated electrode capacity ($C_{\text{an}}^{\text{est}}, C_{\text{cat}}^{\text{est}}$) and linear shifting by an offset ($\beta_{\text{an}}, \beta_{\text{cat}}$) [24,37]:

$$Q_{\text{cat},\text{full}} = C_{\text{cat}}^{\text{est}} \cdot (1 - f_{\text{cat}}^{-1}(U_{\text{cat}})) + \beta_{\text{cat}} = f_{\text{cat},\text{full}}^{-1}(U_{\text{cat}}, \theta) \quad (5)$$

$$Q_{\text{an},\text{full}} = C_{\text{an}}^{\text{est}} \cdot (f_{\text{an}}^{-1}(U_{\text{an}})) + \beta_{\text{an}} = f_{\text{an},\text{full}}^{-1}(U_{\text{an}}, \theta) \quad (6)$$

The alignment parameters used for scaling and shifting of the OCP curves are collectively denoted as

$$\theta = [C_{\text{an}}^{\text{est}}, C_{\text{cat}}^{\text{est}}, \beta_{\text{an}}, \beta_{\text{cat}}]. \quad (7)$$

$f_{\text{cat},\text{full}}(Q, \theta)$ and $f_{\text{an},\text{full}}(Q, \theta)$ then describe the OCP of the electrodes as a function of absolute charge in the coordinate system of the partial charging curve. The half-cell OCP curves are taken from [48] and are implemented as lookup tables. The full-cell OCV curve is reconstructed as the difference between the transformed half-cell curves

$$U_{\text{OCV}}^{\text{est}}(Q, \theta) = f_{\text{cat},\text{full}}(Q, \theta) - f_{\text{an},\text{full}}(Q, \theta). \quad (8)$$

The alignment parameters are obtained by minimizing the sum of square errors (SSE) between the measured partial OCV curve and the reconstructed OCV curve in the range between the beginning $Q = 0 \text{ Ah}$ and the end of the partial charging curve $Q = Q_{\text{partial}}$:

$$\arg \min_{\theta} \text{SSE} = (U_{\text{OCV}}^{\text{est}}([0 \text{ Ah}, Q_{\text{partial}}], \theta) - U_{\text{OCV}}([0 \text{ Ah}, Q_{\text{partial}}]))^2 \quad (9)$$

The nonlinear programming solver *fmincon* using the interior-point algorithm implemented in MATLAB® is used for the optimization. The optimization is performed subject to the constraint that the reconstructed OCV curve reaches at least a value of 4.2 V at the end of charging

$$U_{\text{OCV}}^{\text{est}}(Q_{\text{max}}) \geq 4.2 \text{ V}, \quad (10)$$

where Q_{max} is the end of the overlapping part of the transformed half-cell curves. A similar approach is suggested in [8]. A typical result of an OCV curve reconstruction based on a partial charging curve is shown in Fig. 1(c). The difference between absolute voltages is used as a cost function for the optimization in this study. The DV of the reconstructed OCV curve also fits the DV of the measured voltage well in cases where the fitting in the voltage domain is successful. An example of this is shown in Fig. 1(d).

The initial values and boundaries for the alignment parameter optimization are set according to Table 2. For the cases in which C/30 curves of aged cells from the aging test sequence are reconstructed, the results for the alignment parameters obtained for the preceding iteration are used as initial values [37] and the boundaries are chosen to allow 30% of variation from this value, as long as the absolute boundary values listed in Table 2 are not exceeded. As can be seen in Table 2, the initial values for β_{an} and β_{cat} depend on an estimate for the initial SOC of the partial charging curve. This estimated initial SOC ($SOC_{\text{min}}^{\text{est}}$) is calculated as

$$SOC_{\text{min}}^{\text{est}} = SOC(U_{\text{OCV}}(0 \text{ Ah})) \quad (11)$$

where $SOC(U)$ is an interpolation of the pristine SOC-OCV curve and $U_{\text{OCV}}(0 \text{ Ah})$ is the first voltage value contained in the partial charging curve compensated by the overpotential offset. The pristine SOC-OCV curve is calculated as the average of the normalized C/30 charging curves measured for the individual cells during the first charging rate test. We would like to emphasize that this estimate on the start SOC is solely used to set the initial values for β_{an} and β_{cat} . The final values for these parameters are obtained during the optimization step. A low estimation accuracy of $SOC_{\text{min}}^{\text{est}}$ therefore has no significant impact on the accuracy of the capacity and degradation mode estimation.

Based on the complete reconstructed OCV curve, the cell capacity $C_{\text{C}/30}^{\text{est}}$ can be calculated [8] according to

$$C_{\text{C}/30}^{\text{est}} = Q_{\text{OCV}}^{\text{est}}(U_{\text{eval,max}}) - Q_{\text{OCV}}^{\text{est}}(U_{\text{eval,min}}), \quad (12)$$

where $Q_{\text{OCV}}^{\text{est}}(U)$ is the inverse of the reconstructed OCV curve and $U_{\text{eval,min}}$ and $U_{\text{eval,max}}$ are the voltage limits between which the C/30 charging capacity is defined in this study. The definition of $C_{\text{C}/30}^{\text{est}}$ is shown diagrammatically in Fig. 1(c). $U_{\text{eval,max}} = 4.2 \text{ V}$ is the upper cut-off voltage during charging and was chosen according to the specifications of the cell manufacturer. For $U_{\text{eval,min}}$ the value of 3.248 V is chosen based on the following consideration: during the experiments, the cells were CC discharged to 2.5 V prior to the C/30 charging procedure but the measured charging curves do not start at this value as the voltage relaxes towards higher values during the relaxation time before the charging phase. The minimum voltage value of the charging curve also generally increases with aging as the internal resistance and therefore the overpotential at the end of the discharging phase increases. In order to have a consistent measured reference for the cell capacity and the OCV (C/30) curve at all aging states, we use $U_{\text{eval,min}} = 3.248 \text{ V}$, the highest minimum value of all C/30 charging curves, as the starting point for the capacity calculation and reconstructed OCV curve evaluation. The reference capacity $C_{\text{C}/30 \text{ ch}}$ is then calculated as the charge throughput measured between $U_{\text{eval,min}}$ and $U_{\text{eval,max}}$ during the C/30 charging phase.

The second output of the algorithm is the reconstructed OCV curve itself, which could for example be used to update the OCV curve used by a BMS for SOC estimation during aging. To decouple the evaluation of the accuracy of the shape of the reconstructed OCV curve from the accuracy of the capacity estimation, both the reference curve and the curve calculated with the algorithm are normalized in the charge dimension

$$U_{\text{OCV,eval}}^{\text{est}}(Q') = U_{\text{OCV}}^{\text{est}}([Q_{\text{OCV}}^{\text{est}}(U_{\text{eval,min}}), Q_{\text{OCV}}^{\text{est}}(U_{\text{eval,max}})]) \quad (13)$$

$$U_{\text{OCV,eval}}(Q') = U_{\text{OCV}}([Q_{\text{OCV}}(U_{\text{eval,min}}), Q_{\text{OCV}}(U_{\text{eval,max}})]) \quad (14)$$

Table 2

Initial values and boundaries for the alignment parameters.

Parameter	Initial value	Lower boundary	Upper boundary
C_{an}^{est}	3.45 Ah	2.21 Ah	3.67 Ah
C_{cat}^{est}	3.82 Ah	2.35 Ah	4.02 Ah
β_{an}	$(0.02 - SOC_{min}^{est}) \cdot 3.45$ Ah	-3.67 Ah	0 Ah
β_{cat}	$(0.13 - SOC_{min}^{est}) \cdot 3.82$ Ah	-4.02 Ah	0 Ah

where Q' is a vector of $n = 2000$ equally spaced interpolation points between 0 and 1 at which the difference between the reconstructed and measured curve is evaluated. As a measure for the accuracy of the reconstructed OCV curve we use the root mean square error (RMSE) between the reconstructed OCV curve and the measured C/30 charging curve in the voltage range between $U_{eval,min}$ and $U_{eval,max}$, denoted as ϵ_{OCV} :

$$\epsilon_{OCV} = \sqrt{\frac{1}{n} (U_{OCV,eval}^{est}(Q') - U_{OCV,eval}(Q'))^2}. \quad (15)$$

Finally, the accuracy of the results in respect of the electrode capacities (C_{an}^{est} , C_{cat}^{est}) and the lithium inventory (C_{lit}^{est}) is evaluated. C_{an}^{est} and C_{cat}^{est} are direct output parameters of the optimization procedure, the lithium inventory is calculated as the difference in charge between the end of the cathode OCP curve where the cathode is delithiated and the beginning of the anode OCP curve where the anode is delithiated [33].

The algorithm is applied to parts of the C/30 charging curves measured during the aging test sequence. It is also applied to the CC charging curves at higher current rates measured during the extended charging rate test to study the accuracy of the method at higher charging rates. Before the charging data is processed by the algorithm, it is resampled at equidistant Q values corresponding to a sample frequency of 1 Hz (the original sampling was conducted in a voltage-based manner at a voltage change of 0.5 mV) and filtered by applying a Savitzky–Golay filter with polynomial order of five and a frame length of 71 data points three times. A section of the charging curve is cut out to simulate the scenario where only a part of the charging curve can be measured in an application. The actual capacity measured during the charging phase is used for calculating the SOCs for cutting out the partial curves. For the extended charging rate tests, this also includes the CV phase.

The RMSE of the algorithm output quantities (X^{est}) for all cells and all periods of the aging test sequence (until SOH = 80%) is used as a measure of the accuracy of the algorithm for different SOC windows. It is calculated according to

$$RMSE(X^{est}) = \sqrt{\frac{1}{N} \sum_{i=1}^{n_{cell}} \sum_{j=1}^{n_{period}} (X_{i,j}^{est} - X_{i,j})^2}, \quad (16)$$

where $X_{i,j}^{est}$ is the estimate for the respective output quantity ($C_{C/30\ ch}^{est}$, C_{an}^{est} , C_{cat}^{est} , C_{lit}^{est}) of the i th cell in the j th period of the aging test sequence. $X_{i,j}$ is the corresponding reference value, i.e., the measured $C_{C/30\ ch}$ of the i th cell in the j th period or the respective value for C_{an} , C_{cat} or C_{lit} that is obtained from the complete C/30 charging curve of the i th cell in the j th period. $n_{cell} = 10$ is the total number of cells and n_{period} the total number of analyzed charging curves of each individual cell until SOH = 80%. N is the total number of analyzed charging curves for all cells. The RMS of ϵ_{OCV}

$$RMS(\epsilon_{OCV}) = \sqrt{\frac{1}{N} \sum_{i=1}^{n_{cell}} \sum_{j=1}^{n_{period}} (\epsilon_{OCV,i,j})^2}, \quad (17)$$

where $\epsilon_{OCV,i,j}$ is the RMSE of the reconstructed OCV curve of the i th cell in the j th period of the aging test sequence, is used as a measure of the accuracy of the OCV curve reconstruction throughout aging.

Similar measures are used to describe the accuracy of the algorithm for different SOC windows at higher charging rates with the difference

that there are only six analyzed cells and that there is only one charging curve per cell, which is the curve obtained during the extended charging rate test.

Using the proposed algorithm in a BMS or for the analysis of field data would be possible by implementing the following additional steps: first, the CC charging phases need to be detected and cut out from the measurement data. This implies that measurement data of current and voltage during charging phases need to be temporally stored. Then, the current is integrated over the time of the charging process to generate the charge throughput vector that is provided to the algorithm along with the corresponding terminal voltage vector. A section at the begin of the charging phase would need to be discarded as discussed in Section 4.2. In addition, another algorithm for determining the resistance values from dynamic operation data, such as the one proposed by Ludwig et al. [49], would needed to be implemented. The updated resistance value at a middle SOC as well as the relevant section of the charging curve would then be provided to the algorithm and processed as described in this section.

4. Results and discussion

4.1. Aging analysis based on complete low-current charging curves

In this section, the results of the aging test sequence and the algorithm output for the reference case, where the complete C/30 charging curves are used as input, are presented and discussed.

The discharging capacity measured during the capacity tests ($C_{C/5\ dch}$) is plotted in Fig. 2(a) as a function of total charge throughput. The capacity decreases for all cells with significant differences in the rate of capacity decrease depending on the operating conditions during the continuous cycling periods. The capacity of the cells that are cycled in a limited voltage window (2.5 V–4.0 V and 3.6 V–4.2 V) decreases more slowly over equivalent full cycles when compared to the cells that are cycled in the full voltage range (2.5 V–4.2 V and WLTP). Schindler et al. also observed an extension of the cycle life upon limitation of the upper cut-off voltage for cells of this type [50]. They also measured a similar aging rate for cells of the same type cycled over the full voltage range. The internal pulse resistance $R_{C/3\ ch}$ measured during the pulse tests is shown in Fig. 2(b) as a function of total charge throughput. Analogously to the capacity decrease, the cells that are cycled over the full voltage range exhibit a quicker increase in internal resistance than the cells that are cycled within a limited voltage range.

The cells cycled over the full voltage range reach heavily degraded states during the experiments. The end of life (EOL) of a lithium-ion cell is usually defined as reached when the capacity-based SOH has dropped below 80%. In this study, we define the SOH as $C_{C/5\ dch}/C_{nom}$. As shown in Fig. 2(a), the cells cycled over the full voltage range reach this EOL definition after approximately 570 EFC. The algorithm is only applied to cases where the SOH is above 80% in this study. In principle, the proposed algorithm could also be applied to cells at SOH below 80%, but for the analysis of accuracy and impact of available SOC window and current rate, we concentrate on the case above 80% SOH, because this represents the most important scope of application, as heavily degraded cells at SOH below 80% would not continued to be used in most applications. All charging curves for which the SOH is below 80% are therefore excluded for the following analysis. The number of charging curves above 80% SOH for the individual cells are listed in Table A.1.

The C/30 charging capacity measured between 3.248 V and 4.2 V ($C_{C/30\ ch}$) is used as reference for the capacity estimation as explained in Section 3. The results for $C_{C/30\ ch}$ are shown in Fig. 2(c). The absolute values are lower than for $C_{C/5\ dch}$ because only the part of the capacity above 3.248 V is considered but the trends of the capacity decrease are the same as for $C_{C/5\ dch}$. Applying the algorithm presented in Section 3 to the complete C/30 charging curves at different aging states yields reconstructed OCV curves that are a good fit to the

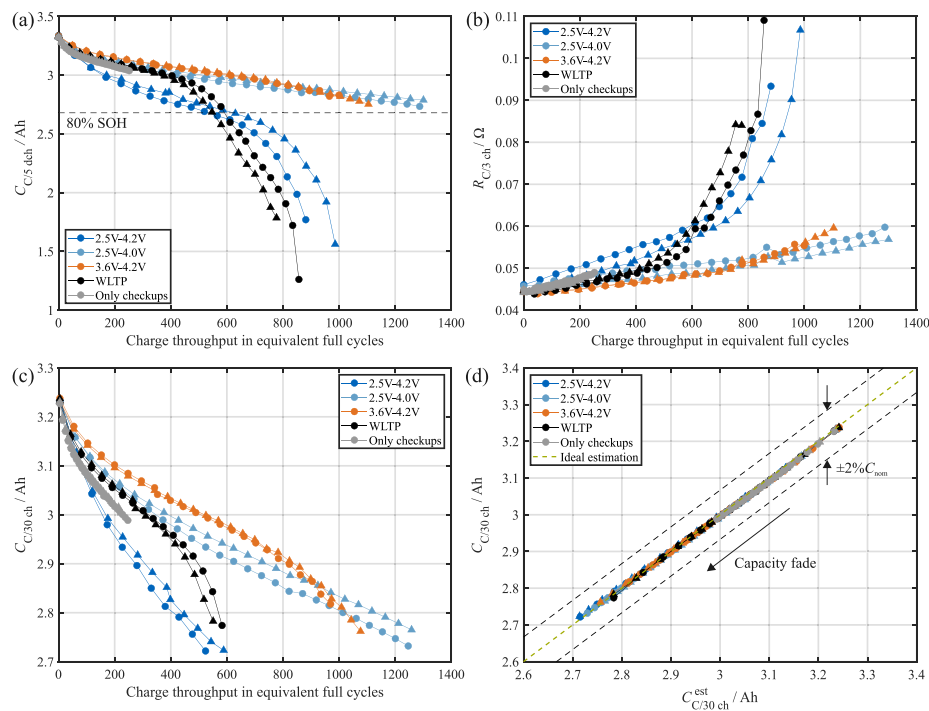


Fig. 2. (a) CC discharging capacity measured at C/5 during the capacity tests as part of the aging test sequence. The different symbols indicate results for the two cells tested under each aging condition. (b) C/3 charging pulse resistance (10 s pulse duration) at 50% SOC measured during the pulse tests. (c) C/30 charging capacity between 3.248 V and 4.2 V ($C_{C/30 \text{ ch}}$) measured during the charging rate tests until 80% SOH. (d) Correlation between measured C/30 charging capacity and C/30 charging capacity estimated with the algorithm at different aging states for the case in which the complete C/30 charging curves are used as input.

measured curves. The $\text{RMS}(\epsilon_{\text{OCV}})$ for all considered charging curves is 3.6 mV and ϵ_{OCV} is always below 7 mV. This means that the proposed OCV model is suitable for reproducing the shape of the OCV curve throughout aging and for different aging conditions. In Fig. 2(d), the correlation between the estimated and the measured C/30 charging capacity is shown. The $\text{RMSE}(C_{C/30 \text{ ch}}^{\text{est}})$ for all cells and aging states is 0.2% C_{nom} and the capacity estimates shown in 2(d) are near to the ideal estimation line ($C_{C/30 \text{ ch}}^{\text{est}} = C_{C/30 \text{ ch}}$). This means that the capacity can be accurately calculated with the proposed algorithm if the complete C/30 charging curves are available.

The degradation modes occurring during aging of the individual cells are calculated from the results for the electrode capacities and the lithium inventory as

$$\text{LAM}_{\text{an}} = \frac{C_{\text{an,inj}} - C_{\text{an}}}{C_{\text{an,inj}}} \quad (18)$$

$$\text{LAM}_{\text{cat}} = \frac{C_{\text{cat,inj}} - C_{\text{cat}}}{C_{\text{cat,inj}}} \quad (19)$$

$$\text{LLI} = \frac{C_{\text{lit,inj}} - C_{\text{lit}}}{C_{\text{lit,inj}}}, \quad (20)$$

where the subscript “inj” refers to the value obtained for the C/30 charging curve in the initial state. The results for LAM_{an} are shown in Fig. 3(a). The change in LAM_{an} as a function of charge throughput differs for the different aging conditions while the two cells aged under the same conditions show comparably similar results. The same applies to the LAM_{cat} shown in Fig. 3(c) and the LLI shown in Fig. 3(e). LAM_{an} and LLI are higher than LAM_{cat} for all aging conditions, which means that cell degradation is primarily driven by these two degradation modes. Similar results have previously been found for this cell type [33, 45, 51, 52].

The shape of the half-cell OCP curves is considered invariant during aging in the algorithm presented in this study, even though it has been shown that this assumption is only approximately valid for silicon-graphite blend anodes [48]. The LAM_{an} is therefore probably overestimated by the order of a few percentage points while LAM_{cat}

and LLI are probably underestimated by the order of a few percentage points [33]. The change in shape of the silicon-graphite OCP curve could theoretically be considered in the algorithm by using a blend electrode model and adding another optimization parameter describing the remaining anode capacity ratio provided by the silicon [33]. This is not done here, because adding another optimization parameter results in lower robustness of the fitting algorithm if partial charging curves are used as input, which would be a challenge in applications.

In Figs. 3(b), 3(d) and 3(f) the degradation modes are plotted with respect to the remaining cell capacity $C_{C/5 \text{ dch}}$. This representation shows that the difference between the degradation modes for cells at the same SOH is always below 4 percentage points even though they are aged under different conditions. We interpret this finding in such a way that the different degradation modes are triggered in an approximately fixed ratio that is only slightly influenced by the applied aging conditions. Further research is needed to obtain quantitative results on this topic and to investigate whether this result can be generalized to other aging conditions and cells.

4.2. Accuracy of the method for partial charging curves

In this section, the accuracy of the estimated remaining cell capacity, OCV reconstruction and estimated degradation modes is analyzed for the case in which only parts of the C/30 charging curves measured during the aging test sequence are used as input for the algorithm.

Fig. 4(a) shows the $\text{RMSE}(C_{C/30 \text{ ch}}^{\text{est}})$ for all cells and aging states for different SOC windows used for the OCV reconstruction. In this representation, each field of the matrix corresponds to a certain SOC window defined by the SOC at which the partial curve begins (SOC_{\min} , indicated on the X-axis) and the SOC at which the partial curve ends (SOC_{\max} , indicated on the Y-axis). The numeric value for the RMSE of the capacity estimation obtained from the OCV reconstruction based on a certain SOC window is indicated in the corresponding field of the matrix. The estimation accuracy is also visualized by a color code, where blue corresponds to high accuracy and yellow to low accuracy.

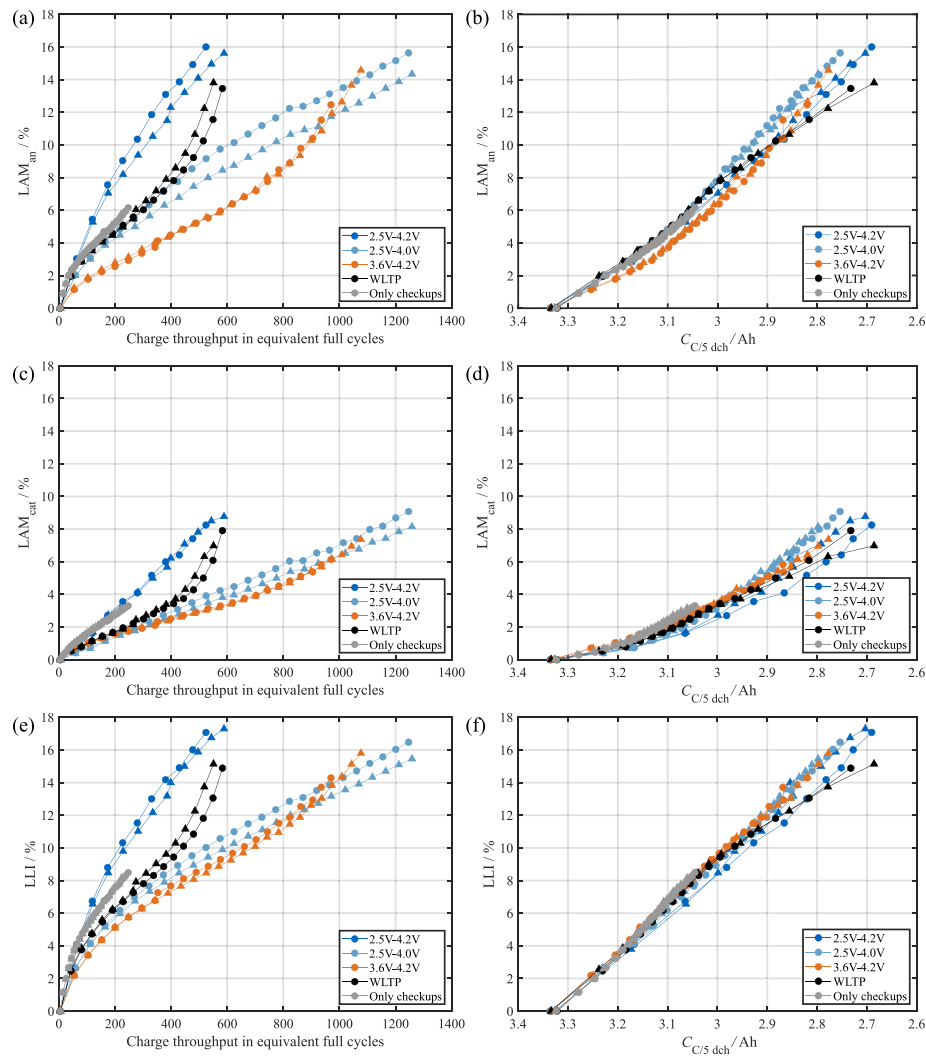


Fig. 3. Reference values for the degradation modes obtained from complete C/30 charging curves. The different symbols represent results for the two cells aged under the same conditions. (a) LAM_{an} as a function of total charge throughput. (b) LAM_{an} as a function of the remaining C/5 discharging capacity. (c) LAM_{cat} as a function of total charge throughput. (d) LAM_{cat} as a function of the remaining C/5 discharging capacity. (e) LLI as a function of total charge throughput. (f) LLI as a function of the remaining C/5 discharging capacity.

As visible in Fig. 4(a), the accuracy of the capacity estimation strongly depends on the SOC window of the partial charging curve provided to the algorithm. The position of the bluish area in Fig. 4(a) reveals that SOC_{min} needs to be less than or equal to 20% in order to obtain capacity estimates with high accuracy ($\text{RMSE}(C_{\text{30 ch}}^{\text{est}}) \leq 2.0\%$). We assume that the reason for the algorithm failing at SOC_{min} above 20% is that the information on the position of the stage 2L graphite phase is necessary to obtain an accurate estimate for the anode capacity, which is also limiting for the full-cell capacity at low cell voltages. This can be seen in Fig. 4(c) where the DV of a pristine cell is shown and the peaks are associated with phases of the electrode materials [51,53,54]. If partial charging curves with SOC_{min} greater than 20% are used, the anode capacity, and as a consequence also the cell capacity, are heavily overestimated. Similar results were obtained by Yang et al. [37]. Also Marongiu et al. [2,3] reported that the length and position of voltage plateaus corresponding to the 2L-2 and 2-1 phase transitions of the graphite need to be observable in order to obtain accurate capacity estimation based on the reconstruction of partial charging curves.

In addition to starting at a low SOC_{min}, the partial charging curves should comprise at least 30% of the actual cell capacity to provide enough information for accurate capacity estimation. For cases where SOC_{min} is between 5% and 20%, the accuracy of the capacity estimation increases with an increase in the width of the SOC window used

until SOC_{max} of approximately 60%. The proposed algorithm should therefore preferably be applied to charging curves comprising at least the window between 20% and 60% SOC to enable accurate capacity estimation throughout aging. As an example of the capacity estimation for cells aged under different conditions and at different aging stages, the correlation between estimated and measured capacity is shown in 4(d) for the case where partial charging curves in the SOC window between 15% and 75% are used. It can be seen that the deviation from the ideal estimation is smaller than 2% C_{nom} in most cases.

In Fig. 4(b), the RMS(ϵ_{OCV}) for all cells and aging states is shown as a measure of the accuracy of the reconstruction of the shape of the aged OCV curve from partial charging curves with different SOC windows. Analogous to the accuracy of the capacity estimation, the obtained accuracy of the reconstructed OCV curve shape strongly depends on the SOC window used. Reconstructed complete OCV curves with high accuracy ($\text{RMS}(\epsilon_{\text{OCV}}) \leq 6.2 \text{ mV}$) can be obtained if a window extending between 20% SOC and 70% SOC at least is used. As for the capacity estimation, the necessity for a SOC_{min} $\leq 20\%$ arises from the need to have at least a part of the 2L graphite stage inside the analyzed part of the charging curve in order to obtain accurate estimates on the anode capacity. The necessity of an SOC_{max} $\geq 70\%$ for accurate OCV construction differs from the requirements for the capacity estimation, where accurate estimates can also be obtained with a lower SOC_{max}.

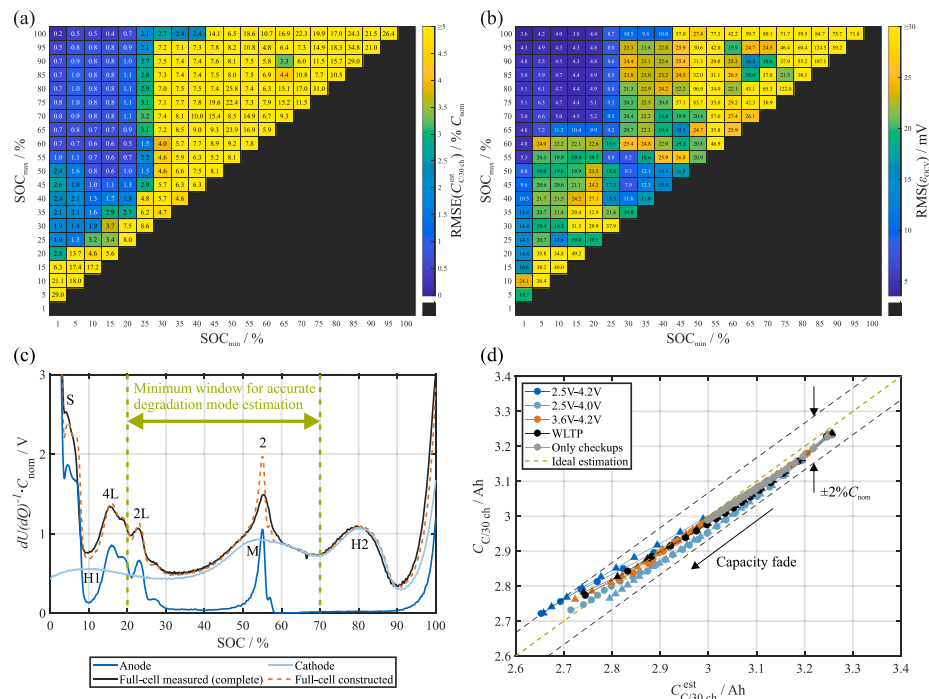


Fig. 4. (a) RMSE of the C/30 charging capacity estimates for all cells and aging states for partial curves with different SOC windows. (b) RMS of the RMSE of the reconstructed OCV curves (ϵ_{OCV}) for all cells and aging states for partial curves with different SOC windows. (c) Measured and reconstructed DV of a pristine cell. The peaks of the DV are associated with phases of the electrode materials: Graphite stages 4L, 2L and 2 [53], a silicon phase S [51] and NMC-811 phases H1, M and H2 [54]. (d) Correlation between measured C/30 charging capacity and C/30 charging capacity estimated using the algorithm based on partial C/30 charging curves between 15% and 75% SOC at different aging states. (For interpretation of the references to color in this figure legend, the reader is referred to the web version of this article.)

The RMSE of the estimated anode capacity, cathode capacity and lithium inventory based on partial charging curves with different SOC windows is shown in Figs. 5(a)–5(c). The estimation accuracy results are presented as a percentage of the respective mean value obtained for the complete charging curves in the pristine state ($C_{\text{an,in},\text{mean}}$, $C_{\text{cat,in},\text{mean}}$, $C_{\text{lit,in},\text{mean}}$). As for the reconstruction of the OCV curve, accurate estimates for the anode capacity ($\text{RMSE}(C_{\text{an}}^{\text{est}}) \leq 2.2\% C_{\text{an,in},\text{mean}}$) are obtained for $\text{SOC}_{\text{min}} \leq 20\%$ and $\text{SOC}_{\text{max}} \geq 70\%$. Estimation of the cathode capacity with high accuracy ($\text{RMSE}(C_{\text{cat}}^{\text{est}}) \leq 1.0\% C_{\text{cat,in},\text{mean}}$) is also only possible for cases where $\text{SOC}_{\text{max}} \geq 70\%$ but comparably accurate results on the cathode capacity can also be obtained if only the upper part of the SOC range, for example between 60% and 90% is available. Accurate estimation of the lithium inventory ($\text{RMSE}(C_{\text{lit}}^{\text{est}}) \leq 2.1\% C_{\text{lit,in},\text{mean}}$) can be obtained if SOC_{min} is not greater than 20% and if the width of the used SOC window is at least 25% of the actual cell capacity.

Accurate OCV reconstruction and electrode capacity estimation is only possible if $\text{SOC}_{\text{max}} \geq 70\%$. This means that even though accurate capacity estimates can be obtained for $\text{SOC}_{\text{max}} \leq 70\%$, the reconstruction of the complete curve is only performed correctly if the middle SOC range, where the graphite stage 2 and the NMC-811 M phase are located (see Fig. 4(c)), is included in the analyzed partial charging curve. If this is not the case, the cathode capacity is increasingly underestimated and the anode capacity is increasingly overestimated during aging. Nevertheless, the estimation of the lithium inventory is comparably accurate as can be seen in Fig. 5(c). This is because the cathode is identified as limiting the cell capacity at 100% SOC with cathode capacity reserves below 0% SOC and the anode is identified as limiting the cell capacity at 0% SOC with anode capacity reserves above 100% SOC as shown in Fig. 5(d). Neither the overestimated part of the anode capacity nor the underestimated part of the cathode capacity contribute to the cell capacity or the lithium inventory, therefore an

erroneous estimation of these quantities does not lead to a huge error in the full-cell capacity estimation.

Another phenomenon that can be observed is that in some cases the estimation accuracy of the cell capacity and the electrode capacities, as well as the OCV reconstruction accuracy is slightly reduced if the SOC range between 5% and 15% is included in the algorithm input. This results from an underestimation of both anode and cathode capacity for aged cells if this SOC range is included. A possible reason for this phenomenon is that the OCV model that is used by the algorithm might be less accurate for aged silicon-graphite at low lithiation because the probable increase in inhomogeneous lithiation [30] and a change in the capacity contribution of silicon [33,48] are not considered in the model. The algorithm still tries to align the measured and simulated full-cell OCV curves in this SOC region, which leads to a reduced overall estimation accuracy. Reduced estimation accuracy is not observed if the begin of charge is also included in the algorithm input, as the fitting is dominated by the steep increase of the OCV curve at the begin of charge in this case.

Summing up the results concerning the accuracy of OCV reconstruction based on partial C/30 CC charging curves, it can be stated that for the investigated cell type, accurate capacity estimation and estimation of the lithium inventory is possible throughout aging if the charging curve starts at or below 20% SOC and lasts for at least 30% of the actual cell capacity. Accurate reconstruction of the OCV curve and estimation of the electrode capacities is only possible under the additional condition that the cell is charged up to an SOC of at least 70%. Similar results were reported by Yang et al. who used a similar algorithm and found that SOH estimation with a relative error of ±2.5% is possible as long as the partial charging curve contains the SOC range from 20% to 70% [37]. It should be noted that in real applications, a partial charging curve is not obtained as a segment of a complete charging curve but measured during an actual partial charging process,

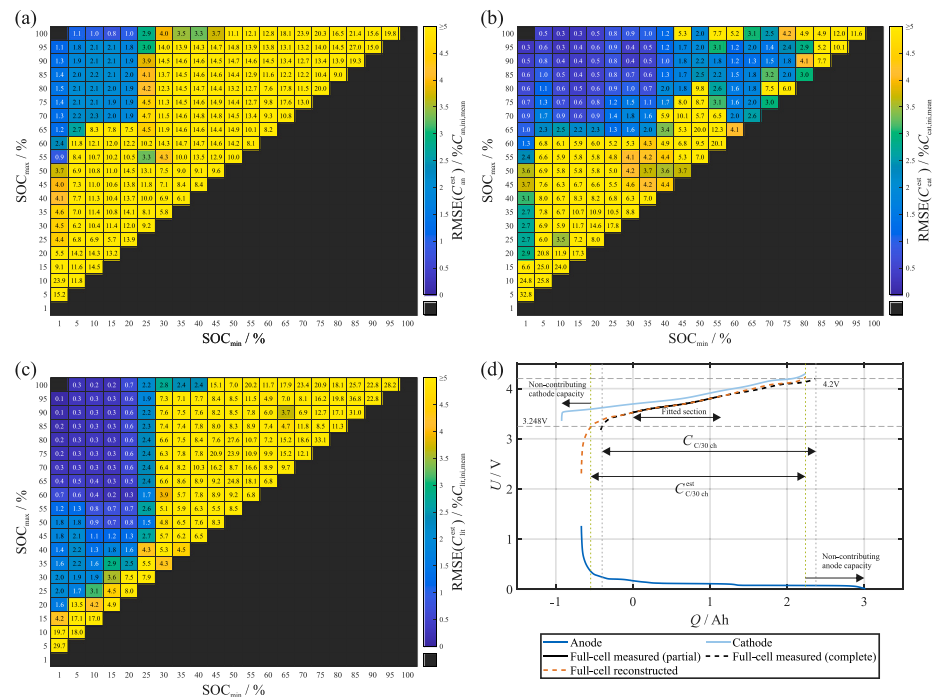


Fig. 5. (a) RMSE of the estimated anode capacity for all cells and aging states based on partial C/30 charging curves with different SOC windows as input. (b) RMSE of the estimated cathode capacity for all cells and aging states based on partial C/30 charging curves with different SOC windows as input. (c) RMSE of the estimated lithium inventory for all cells and aging states based on partial C/30 charging curves with different SOC windows as input. (d) Result for fitting a charging curve between 15% and 55% SOC of an aged cell (cycled between 3.6 V–4.2 V up to 82.9% SOH).

in which the overpotential builds up at the start of the charging. Findings have demonstrated that the section of the charging curve in which the overpotential builds up, should be discarded from the input for OCV reconstruction [21,37]. Consequently, a lower SOC_{min} than indicated by our results is probably needed in applications to compensate for the discarded section.

In this study, we investigate charging phases where the cells have been at rest at the begin of charge. In principle, the algorithm should also be applicable to charging phases where the cell had not been at rest at the begin of charge. In this case, the section at the begin of charge in which the terminal voltage is significantly influenced by overpotentials resulting from the operation prior to the charging phase has to be excluded from the algorithm input.

4.3. Accuracy of the method at higher charging rates

In this section, the accuracy of the capacity estimation, OCV reconstruction and degradation mode estimation is evaluated for the case, where charging rates higher than C/30 from the extended charging rate test are used as input. There are two general problems for applying OCV reconstruction to charging curves at higher rates: first, the overpotential that builds up during the charging process is higher than for the low-current case and can therefore not be neglected. In this study we consider this overpotential by subtracting a constant voltage offset from the charging curves as described in Section 3. Using this simple electrical model for overpotential compensation has the advantage of simple parametrization. In our case, it is sufficient to extract a pulse resistance at a middle SOC from time to time to update the scalar value of $R_{\text{C}/30\text{ ch}}$, which we consider to be feasible in most applications. The determination of an SOC-dependent resistance would be significantly more complex. Another advantage of using an SOC-independent resistance value for polarization compensation is that the shape of the

measured charging curve is not affected by the compensation. Using an SOC-dependent resistance could introduce additional features to the compensated charging curve that are not contained in the measured curve. Contrary to this, using an SOC-dependent resistance value could possibly improve the accuracy of the overpotential compensation in SOC regions where the resistance significantly differs from the value at 50% SOC. For the investigated cell type, this would mainly apply to the region below 20% SOC [55].

The second main problem is that the lithiation/delithiation of the electrodes is increasingly inhomogeneous at higher charging rates which hinders the determination of the electrode capacities. The DV of the CC charging procedures at different rates as part of the extended charging rate test performed on a pristine cell is shown in Fig. 6(a). The inhomogeneous lithiation of the anode at higher charging rates results in a broadening of the anode DV peaks as can be seen in Fig. 6(a). The central anode DV peak corresponding to the graphite stage 2 is not visible if the cells are charged at 0.264 C. Similarly, Marongiu et al. reported that the graphite phase transitions are not clearly distinguishable from charging curves measured at current rates above 0.3 C [3].

In Fig. 6(b) the results for $C_{\text{C}/30\text{ ch}}^{\text{est}}$ estimated from complete CC charging curves with different rates are shown for three sample cells at different SOH and with different aging history. The estimated capacities differ increasingly from the measured reference if higher charging rates are used. A capacity estimation with an error of less than 2% C_{nom} is obtained for current rates up to C/6 for the pristine cell. For the cell cycled until an SOH of 84.2%, this accuracy is only obtained for current rates up to C/15. The negative influence of higher current rates on the accuracy of the method therefore increases with cell aging. Detailed results for the capacity estimation accuracy obtained for all cells that were subject to the extended charging rate test are listed in Table 3.

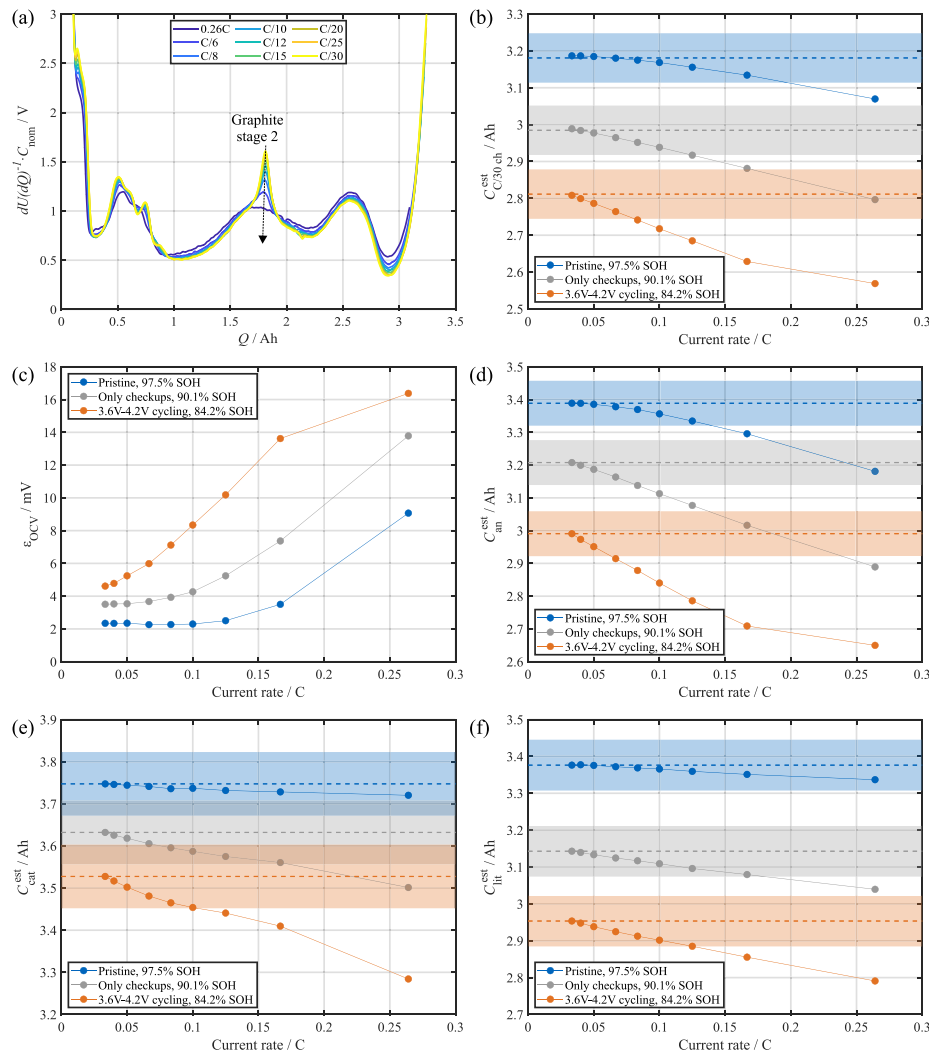


Fig. 6. (a) DV of CC charging curves at different current rates for a pristine cell. (b) Capacities of three sample cells at different aging states estimated using the algorithm including overpotential compensation based on complete charging curves at different current rates. The measured reference values for $C_{30 \text{ ch}}$ are indicated as dashed horizontal lines. The shaded areas indicate the 2% C_{nom} error range. (c) RMSE of the reconstructed OCV curves, (d) anode capacities, (e) cathode capacities and (f) lithium inventory of the three sample cells estimated using the algorithm including overpotential compensation based on complete charging curves at different current rates. The reference values obtained from the complete C/30 charging curves are indicated as dashed horizontal lines in (d-f) and error ranges corresponding to 2% of $C_{\text{an,in,mean}}/C_{\text{cat,in,mean}}/C_{\text{lit,in,mean}}$ are shown as shaded areas.

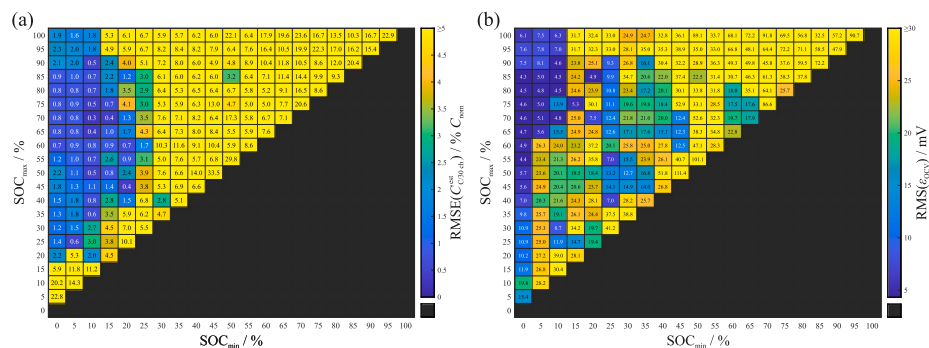


Fig. 7. (a) RMSE of the capacity estimates for six cells (two each at approx. 97%, 90% and 83% SOH) calculated from partial charging curves at C/10 with different SOC windows using overpotential compensation. (b) RMS of the RMSE of the reconstructed OCV curves for the six cells calculated from partial charging curves at C/10 with different SOC windows using overpotential compensation.

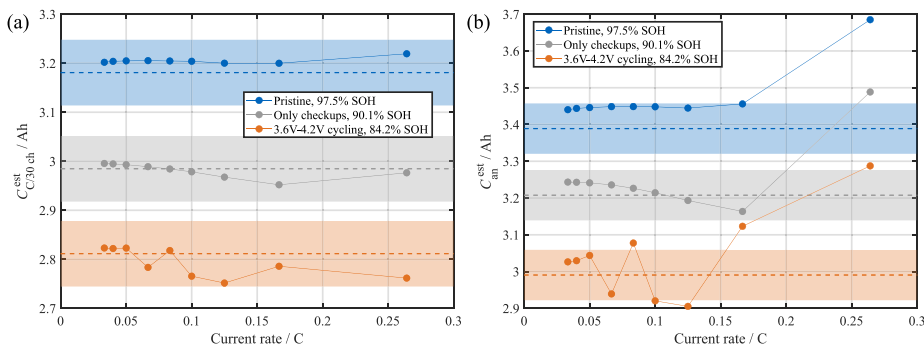


Fig. 8. (a) Capacities of three sample cells at different aging states estimated with the proposed algorithm including overpotential compensation based on partial charging curves (10–80% SOC) at different current rates. The measured values for $C_{\text{C}/30 \text{ ch}}$ which are used as reference are indicated as dashed horizontal lines. The shaded areas indicate the $2\% C_{\text{nom}}$ error range. (b) Anode capacities of the three cells at different aging states estimated with the algorithm including overpotential compensation based on partial charging curves (10–80% SOC) at different current rates. The anode capacities values obtained from the complete $\text{C}/30$ charging curves which are used as reference are indicated as dashed horizontal lines. The shaded areas indicate the $2\% C_{\text{an,in,mean}}$ error range.

Table 3

Capacity estimation error based on complete charging curves at different current rates measured during the extended charging rate test. The results are obtained using overpotential compensation.

Charging rate/C		1/30	1/25	1/20	1/15	1/12	1/10	1/8	1/6	0.264
Cell	SOH/%	Capacity estimation error/% C_{nom}								
Pristine #1	97.5	0.2	0.2	0.1	0.0	0.2	0.4	0.8	1.4	3.3
Pristine #2	97.5	0.1	0.1	0.1	0.0	0.2	0.4	0.7	1.3	3.3
Only checkups #1	90.1	0.1	0.0	0.2	0.6	1.0	1.4	2.0	3.1	5.6
Only checkups #2	90.4	0.1	0.0	0.2	0.6	1.0	1.3	2.0	3.0	5.5
3.6 V-4.2 V #1	82.5	0.1	0.4	0.8	1.6	2.4	3.2	4.3	5.9	7.7
3.6 V-4.2 V #2	84.2	0.1	0.4	0.7	1.4	2.1	2.8	3.8	5.5	7.2

Table 4

Capacity estimation error based on partial charging curves (10–80% SOC) at different current rates measured during the extended charging rate test. The results are obtained using overpotential compensation.

Charging rate/C		1/30	1/25	1/20	1/15	1/12	1/10	1/8	1/6	0.264
Cell	SOH/%	Capacity estimation error/% C_{nom}								
Pristine #1	97.5	0.6	0.7	0.7	0.7	0.7	0.7	0.6	0.6	1.1
Pristine #2	97.5	0.6	0.7	0.7	0.7	0.7	0.7	0.6	0.7	1.2
Only checkups #1	90.1	0.3	0.3	0.2	0.1	0.0	0.2	0.5	1.0	0.2
Only checkups #2	90.4	0.3	0.3	0.3	0.2	0.0	0.1	0.4	0.8	0.1
3.6 V-4.2 V #1	82.5	0.3	0.3	0.2	0.8	0.1	0.1	0.4	0.9	2.0
3.6 V-4.2 V #2	84.2	0.3	0.3	0.3	0.8	0.2	1.4	1.8	0.8	1.5

The accuracy of the OCV estimation ε_{OCV} is shown in Fig. 6(c). Again, the accuracy decreases both with the increase in current rate and cell degradation, but highly accurate OCV reconstruction ($\varepsilon_{\text{OCV}} \leq 6 \text{ mV}$) is possible for the C/6 charging curve of the pristine cell.

As already mentioned, a probable reason for the reduced accuracy of the algorithm results at higher current rates is the increasingly inhomogeneous lithiation of the anode, which hinders the detection of the graphite stages (see Fig. 6(a)) and thus the estimation of the anode capacity. Another reason might be that for higher current rates, the curve alignment gets dominated by a comparably steep voltage increase at the end of charging, which is erroneously interpreted as complete lithiation of the anode but is probably at least partly due to overpotentials that are not correctly compensated by the model. The second aspect can be avoided by leaving out the SOC range above 85% as discussed below.

As visible in Figs. 6(d)–6(f), the accuracy of the estimation of electrode capacities and lithium inventory is also lower at higher current rates, especially for aged cells. The results suggest that accurate anode capacity estimation ($|C_{\text{an}}^{\text{est}} - C_{\text{an}}| \leq 2\% C_{\text{an,in,mean}}$) is possible for charging rates up to C/8 for the pristine cell but only for charging rates up to C/20 for the aged cell. The estimation of the cathode

capacity is less sensitive to increased current rates and an accuracy of $|C_{\text{cat}}^{\text{est}} - C_{\text{cat}}| \leq 2\% C_{\text{cat,in,mean}}$ can be obtained even at 0.264 C for the pristine cell and for current rates up to C/10 for the cell at 84.2% SOH. Similar results are obtained for the accuracy of the estimation of C_{lit} , where $|C_{\text{lit}}^{\text{est}} - C_{\text{lit}}| \leq 2\% C_{\text{lit,in,mean}}$ is reached for current rates up to 0.264 C for the pristine cell and for current rates up to C/8 for the cell at 84.2% SOH. The systematic underestimation of the electrode capacities at higher current rates in comparison to the reference obtained at C/30 might be due to a limited rate capability of the electrodes which also increases with aging [36]. Typical results for one of the cells for each aging history are shown in Figs. 6(b)–6(f) as the results for the respective second cell with the same aging history are similar to the examples shown.

The requirements on the current rate for both capacity estimation and degradation mode analysis are probably different for other cell types. With a nominal volumetric energy density of approximately 696 Wh l^{-1} , the investigated cells are optimized towards high energy and have therefore comparably thick electrode coatings (anode $\approx 85 \mu\text{m}$, cathode $\approx 72 \mu\text{m}$ [43]). This probably results in a comparably inhomogeneous lithiation/delithiation of the electrodes which hinders the OCV reconstruction even at moderate charging rates. Thus, the

charging rate limits might be higher for cell types that are more optimized towards high power.

A comparison between the algorithm results obtained with and without using the overpotential compensation is provided in Fig. C.1 in the appendix. This comparison shows that using the proposed overpotential compensation increases the accuracy of the capacity estimation, the OCV reconstruction and the estimation of $C_{\text{lit}}^{\text{est}}$ in most cases, while it reduces the accuracy of the electrode capacity estimation in most cases.

The combined influence of using both a limited part of the charging curve and a higher current rate is shown in Fig. 7(a). The RMSE ($C_{\text{C}/30 \text{ ch}}^{\text{est}}$) calculated based on the C/10 charging curves of the six cells that underwent the extended charging rate test is shown here as a function of the SOC window used. These results indicate that accurate capacity estimation (RMSE ($C_{\text{C}/30 \text{ ch}}^{\text{est}}$) $\leq 2\% C_{\text{nom}}$) can be obtained if SOC_{min} is not higher than 10% and the width of the SOC window is greater than 20%. In addition to this, the capacity estimation accuracy is higher, if the upper 10% of the SOC window is excluded for the curve alignment. In this SOC region near the end of charging, the measured curves exhibit a steep increase, which is erroneously interpreted to be a feature of the anode OCP but is most probably caused by the overpotential due to the higher current.

In Fig. 7(b) the RMS(ϵ_{OCV}) for the six cells at different aging states is shown for different SOC windows. These results suggest that for accurate OCV reconstruction (RMS(ϵ_{OCV}) $\leq 6\text{ mV}$), SOC_{min} needs to be $\leq 10\%$, and $70\% \leq \text{SOC}_{\text{max}} \leq 85\%$. For $\text{SOC}_{\text{min}} = 0\%$, accurate OCV reconstruction is possible for $45\% \leq \text{SOC}_{\text{max}} \leq 85\%$. In comparison with the capacity estimation, the requirements on the SOC window are therefore stricter if OCV reconstruction and degradation mode analysis is additionally intended. This discrepancy arises from the same source as was found for the partial charging rates at C/30: if $\text{SOC}_{\text{max}} < 70\%$, the electrode capacity estimation is erroneous but neither the underestimated part of the cathode capacity nor the overestimated part of the anode capacity contribute towards the lithium inventory and the cell capacity and therefore these two quantities are still estimated with reasonable accuracy (see Fig. 5(d)).

The sensitivity analysis shows that the window between 10% and 80% SOC is a suitable window for applying the proposed algorithm. In the following, results that can be obtained from charging curves of this example suitable window are discussed. In Fig. 8(a), the results for the capacity estimation based on this SOC window are shown for one example cell of each aging history and for different current rates. If this SOC window is used, accurate capacity estimation with less than $2\% C_{\text{nom}}$ deviation from the reference is achieved for current rates up to 0.264 C even for the aged cell at 84.2% SOH. Similar results are obtained for the other cells with the same aging history. Detailed results for the capacity estimation accuracy based on charging curves between 10–80% SOC at different charging rates are listed in Table 4.

In Fig. 8(b), $C_{\text{an}}^{\text{est}}$ calculated from partial charging curves between 10% SOC and 80% SOC is shown for different current rates for the sample cells. For the aged cell at 84.2% SOH, the estimated values differ by more than $2\% C_{\text{an,inj,mean}}$ for current rates above C/15. At 0.264 C, the anode capacity cannot be accurately estimated even for the pristine cell. This is probably due to the lack of information on the anode phases in the charging curve at this current rate (see Fig. 6(a)).

The restrictions on the applicability of the proposed algorithm are therefore higher if not only the remaining cell capacity but also the degradation modes are to be extracted from partial charging curves at higher charging rates. The accuracy of the algorithm could probably be improved by using a more complex model to consider the overpotential [24,56], but our results show that even with a very simple and easily implementable electrical model, accurate results can be achieved under realistic charging conditions at least in respect of the capacity estimation.

5. Conclusion

We have presented an algorithm for capacity, OCV curve and degradation mode estimation based on CC charging curves that uses the concept of reconstructing OCV curves by fitting pristine half-cell OCP curves to charging curves. The algorithm is easily implemented and no parametrization of an aging model or a correlation between an observable feature and the capacity is necessary. The proposed algorithm is also independent of SOC estimation. We have evaluated the applicability of the algorithm to both partial charging curves and charging curves at higher current rates. For the investigated cell type, the algorithm yields accurate results when applied to partial low-current (C/30) charging curves if the used SOC window comprises at least the range between 20% and 70% SOC.

For the OCV reconstruction based on CC charging curves at higher current rates, the overpotential is compensated by subtracting a constant voltage offset. The accuracy for capacity and degradation mode estimation decreases both with the increase in current rate and with cell degradation. Nevertheless, the algorithm presented in this study yields accurate capacity estimates based on charging curves at current rates up to approximately C/4 even for aged cells if a suitable part of the charging curve (10–80% SOC) is used as input. For an accurate estimation of the degradation modes, charging curves at lower current rates ($\leq \text{C}/15$) are necessary for the investigated cell type. The results show that accurate SOH estimation based on partial charging phases at application-relevant current rates is possible with the presented algorithm for cells at different aging states and which are aged under different conditions. The influence of the charging current amplitude on estimation accuracy probably depends on the cell design which should be further investigated in the future.

Furthermore, we show that for the investigated cell, the aging conditions only have a limited impact on the degradation modes as a function of remaining cell capacity. The different aging conditions lead to different rates of cell degradation but the degradation modes occur in a similar ratio for all investigated aging conditions. Further research is required to investigate whether this finding can be generalized to other aging conditions and cell types.

CRediT authorship contribution statement

Julius Schmitt: Conceptualization, Methodology, Software, Validation, Formal analysis, Investigation, Data curation, Writing – original draft, Visualization, Funding acquisition. **Mathias Rehm:** Software, Writing – review & editing. **Alexander Karger:** Writing – review & editing. **Andreas Jossen:** Writing – review & editing, Supervision, Project administration, Funding acquisition.

Declaration of competing interest

The authors declare the following financial interests/personal relationships which may be considered as potential competing interests: Alexander Karger reports a relationship with TWAICE Technologies GmbH that includes: employment.

Data availability

Datasets related to this article can be found at <https://mediatum.ub.tum.de/1690455>, hosted at the Technical University of Munich [46].

Acknowledgments

This work was supported by the German Federal Ministry for Economic Affairs and Climate Action (grant number 03ETE019F). The responsibility for this publication lies with the authors. Fruitful discussions with Marcel Rogge, Andreas Graule, Julius Bahrke, Marco Fischer and Sven Friedrich are gratefully acknowledged. We would like to thank Lucas Koltermann for the support during the development of the battery electric vehicle profile.

Appendix A. Experimental procedures applied to individual cells

See [Table A.1](#).

Table A.1

Experimental procedures applied to the individual cells. n_{total} is the number of iterations the aging test sequence was applied to an individual cell. n_{period} is the number of charging rate tests at which the SOH is above 80% and that are analyzed in the scope of this study.

Cell	n_{total}	n_{period}	Aging test sequence (applied repeatedly)					Extended charging rate test
			Capacity test	Pulse test	Application phase	Charging rate test	Continuous cycling phase	
2.5 V–4.2 V #1	19	11	Yes	Yes	Yes	Yes	Yes (2.5 V–4.2 V)	No
2.5 V–4.2 V #2	22	13	Yes	Yes	Yes	Yes	Yes (2.5 V–4.2 V)	No
2.5 V–4.0 V #1	26	26	Yes	Yes	Yes	Yes	Yes (2.5 V–4.0 V)	No
2.5 V–4.0 V #2	26	26	Yes	Yes	Yes	Yes	Yes (2.5 V–4.0 V)	No
3.6 V–4.2 V #1	26	26	Yes	Yes	Yes	Yes	Yes (3.6 V–4.2 V)	Yes
3.6 V–4.2 V #2	24	24	Yes	Yes	Yes	Yes	Yes (3.6 V–4.2 V)	Yes
WLTP #1	26	17	Yes	Yes	Yes	Yes	Yes (WLTP)	No
WLTP #2	24	17	Yes	Yes	Yes	Yes	Yes (WLTP)	No
Only checkups #1	26	26	Yes	Yes	Yes	Yes	No (storage)	Yes
Only checkups #2	23	23	Yes	Yes	Yes	Yes	No (storage)	Yes
Pristine #1	0	0	No	No	No	No	No	Yes
Pristine #2	0	0	No	No	No	No	No	Yes

Appendix B. Description of the application phase and the vehicle model

The application phase is designed to simulate typical conditions of battery usage in a battery electric vehicle. The measurement data obtained during the application phase is not discussed in the scope of this study but could for example be used for testing methods for SOC and SOH estimation with dynamic data recorded for cells at different aging states and aged under different conditions.

In each application phase test, the cells were initially fully charged using CCCV charging to 4.2 V with a cut-off current of 50 mA. Afterwards, the application phase with a total duration of three days was started. The application phase contains sections with three types of operating conditions: extended rest times under open-circuit conditions simulating times in which the vehicle is not used (“Rest”); dynamic operation according to a power profile that simulates conditions during driving and regenerative braking based on one of the WLTP phases (“Low”, “Medium”, “High” and “Extra high”); CCCV charging at C/2 to 4.2 V with a cut-off current of 50 mA simulating charging of the vehicle. The sequence in which these sections are combined in the application phase is described in [Table B.1](#). The idea behind this sequence is to have several discharging phases with different depth and SOC window, charging phases with different SOC window and rest times with realistic duration at different SOC level combined in one measurement sequence. An example of the current and voltage measurements obtained during an application phase of a pristine cell is shown in [Fig. B.1](#). Dynamic operation accounts for approximately 12% of the duration of the application phase, while charging accounts for approximately 7% and resting for approximately 81% of the duration.

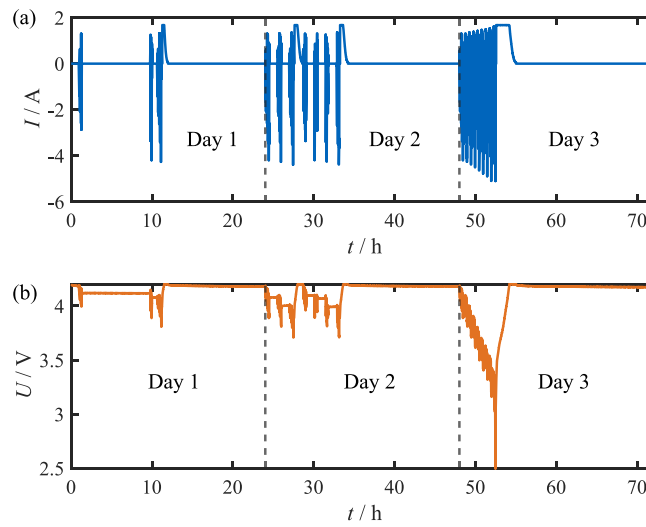


Fig. B.1. Exemplary measurement values obtained during the application phase applied to a pristine cell: (a) applied current, (b) terminal voltage.

The vehicle model that is used to convert the velocity profile of the world harmonized light duty test cycle (WLTC) into a power profile is described in [47, p. 77 ff.]. The implementation of the model used for this study is based on [57]. The parameters used for the vehicle model are described in [Table B.2](#).

Table B.1

Sequence of sections contained in the application phase.

Day	Section	Duration
1	Rest	1 h
	Low	590 s
	Medium	432 s
	Rest	8.5 h
	High	455 s
	Extra high	323 s
	Rest	40 min
	Low	590 s
	Medium	432 s
	High	455 s
	Extra high	323 s
	Rest	5 min
	Charging	approx. 44 min
	Rest	Until a total duration of 24 h is reached
2	Low	590 s
	Medium	432 s
	High	455 s
	Extra high	323 s
	Rest	1 h
	Low	590 s
	Medium	432 s
	High	455 s
	Extra high	323 s
	Rest	1 h
	Low	590 s
	Medium	432 s
	High	455 s
	Extra high	323 s
	Rest	5 min
	Charging	approx. 1 h
	Rest	5 min
	Low	590 s
	Medium	432 s
	High	455 s
	Rest	1 h
	Extra high	323 s
	Low	590 s
	Medium	432 s
	Rest	1 h
	High	455 s
	Extra high	323 s
	Low	590 s
	Rest	1 h
	Medium	432 s
	High	455 s
	Extra high	323 s
	Rest	5 min
	Charging	approx. 1 h
	Rest	Until a total duration of 48 h is reached
3	Low, Medium, High, Extra high	Repeatedly applied until 2.5 V is reached
	Rest	5 min
	Charging	approx. 2.5 h
	Rest	Until a total duration of 72 h is reached

Table B.2

Parameters of the vehicle model used to generate power profiles based on the WLTP velocity profiles.

Parameter	Value
Gravitation	9.81 ms ⁻²
Density of air	1.184 kg m ⁻³
Vehicle mass including battery	1345 kg
Additional mass	100 kg
Air drag coefficient	0.29
Vehicle front area	2.38 m ²
Tire roll resistance factor	0.015
Rotational mass factor	1.05
Additional consumption	1000 W
Motor efficiency	91%
Inverter efficiency	96%

(continued on next page)

Table B.2 (continued).

Parameter	Value
Efficiency factor transmission	90%
Recuperation efficiency	70%
Maximum motor power	125 kW
Maximum recuperation power	50 kW
Number of cells	3456

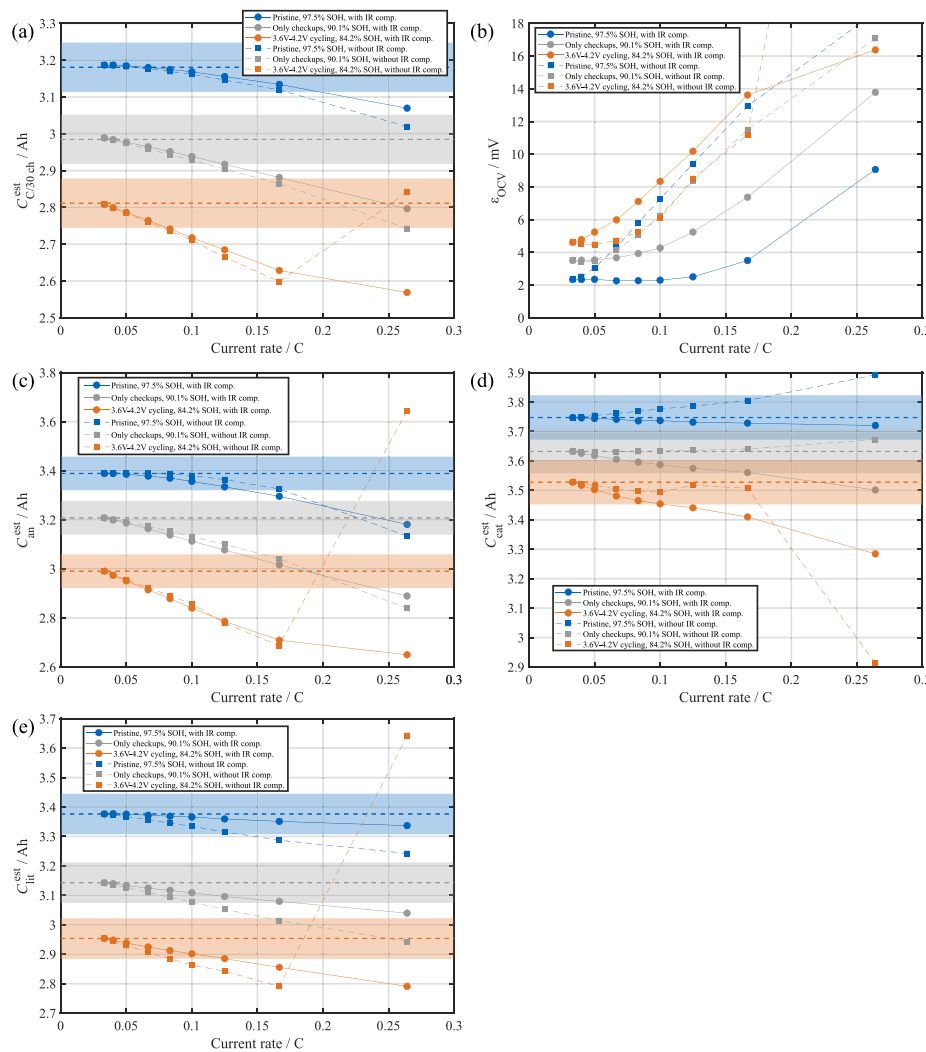


Fig. C.1. (a) Capacities of three sample cells at different aging states estimated using the algorithm with and without overpotential (IR) compensation based on complete charging curves at different current rates. The measured reference values for $C_{30\text{ eh}}$ are indicated as dashed horizontal lines. The shaded areas indicate the 2% C_{nom} error range. (b) RMSE of the reconstructed OCV curves. The data points outside the plotted range are at 0.26C/52 mV ('3.6 V–4.2 V cycling without IR comp.') and 0.26C/18.7 mV ('Pristine without IR comp.'). (c) Anode capacities, (d) cathode capacities and (e) lithium inventory of the three sample cells estimated using the algorithm with and without overpotential compensation based on complete charging curves at different current rates. The reference values obtained from the complete C/30 charging curves are indicated as dashed horizontal lines in (c–e) and error ranges corresponding to 2% of $C_{\text{an,inj,mean}}/C_{\text{cat,inj,mean}}/C_{\text{lit,inj,mean}}$ are shown as shaded areas.

Appendix C. Comparison of algorithm results with and without overpotential compensation

See Fig. C.1.

References

- [1] S. Tong, M.P. Klein, J.W. Park, On-line optimization of battery open circuit voltage for improved state-of-charge and state-of-health estimation, *J. Power Sources* 293 (2015) 416–428, <http://dx.doi.org/10.1016/j.jpowsour.2015.03.157>.
- [2] A. Marongiu, D.U. Sauer, On-board aging estimation using half-cell voltage curves for LiFePO₄ cathode-based lithium-ion batteries for EV applications, *Int. J. Automot. Technol.* 17 (3) (2016) 465–472, <http://dx.doi.org/10.1007/s12239-016-0048-3>.
- [3] A. Marongiu, N. Nlandi, Y. Rong, D.U. Sauer, On-board capacity estimation of lithium iron phosphate batteries by means of half-cell curves, *J. Power Sources* 324 (2016) 158–169, <http://dx.doi.org/10.1016/j.jpowsour.2016.05.041>.
- [4] N. Wassiliadis, J. Adermann, A. Frericks, M. Pak, C. Reiter, B. Lohmann, M. Lienkamp, Revisiting the dual extended Kalman filter for battery state-of-charge

- and state-of-health estimation: A use-case life cycle analysis, *J. Energy Storage* 19 (2018) 73–87, <http://dx.doi.org/10.1016/j.est.2018.07.006>.
- [5] Z. Ma, Z. Wang, R. Xiong, J. Jiang, A mechanism identification model based state-of-health diagnosis of lithium-ion batteries for energy storage applications, *J. Clean. Prod.* 193 (2018) 379–390, <http://dx.doi.org/10.1016/j.jclepro.2018.05.074>.
- [6] X. Li, Z. Wang, L. Zhang, Co-estimation of capacity and state-of-charge for lithium-ion batteries in electric vehicles, *Energy* 174 (2019) 33–44, <http://dx.doi.org/10.1016/j.energy.2019.02.147>.
- [7] S. Lee, J.B. Siegel, A.G. Stefanopoulou, J.-W. Lee, T.-K. Lee, Electrode state of health estimation for lithium ion batteries considering half-cell potential change due to aging, *J. Electrochem. Soc.* 167 (9) (2020) 090531, <http://dx.doi.org/10.1149/1945-7111/ab8c83>.
- [8] S. Lee, P. Mohtat, J.B. Siegel, A.G. Stefanopoulou, J.-W. Lee, T.-K. Lee, Estimation error bound of battery electrode parameters with limited data window, *IEEE Trans. Ind. Inform.* 16 (5) (2020) 3376–3386, <http://dx.doi.org/10.1109/TII.2019.2952066>.
- [9] S. Dey, Y. Shi, K. Smith, A. Colclasure, X. Li, From battery cell to electrodes: Real-time estimation of charge and health of individual battery electrodes, *IEEE Trans. Ind. Electr.* 67 (3) (2020) 2167–2175, <http://dx.doi.org/10.1109/TIE.2019.2907514>.
- [10] M. Dubarry, M. Berecibar, A. Devie, D. Anseán, N. Omar, I. Villarreal, State of health battery estimator enabling degradation diagnosis: Model and algorithm description, *J. Power Sources* 360 (2017) 59–69, <http://dx.doi.org/10.1016/j.jpowsour.2017.05.121>.
- [11] J. Yang, B. Xia, W. Huang, Y. Fu, C. Mi, Online state-of-health estimation for lithium-ion batteries using constant-voltage charging current analysis, *Appl. Energy* 212 (2018) 1589–1600, <http://dx.doi.org/10.1016/j.apenergy.2018.01.010>.
- [12] Y. Li, C. Zou, M. Berecibar, E. Nanini-Maury, J.C.-W. Chan, P. van den Bossche, J. van Mierlo, N. Omar, Random forest regression for online capacity estimation of lithium-ion batteries, *Appl. Energy* 232 (2018) 197–210, <http://dx.doi.org/10.1016/j.apenergy.2018.09.182>.
- [13] R.R. Richardson, C.R. Birk, M.A. Osborne, D.A. Howey, Gaussian process regression for in situ capacity estimation of lithium-ion batteries, *IEEE Trans. Ind. Inf.* 15 (1) (2019) 127–138, <http://dx.doi.org/10.1109/TII.2018.2794997>.
- [14] S. Shen, M. Sadoughi, X. Chen, M. Hong, C. Hu, A deep learning method for online capacity estimation of lithium-ion batteries, *J. Energy Storage* 25 (2) (2019) 100817, <http://dx.doi.org/10.1016/j.est.2019.100817>.
- [15] J. Schmitt, B. Kraft, J.P. Schmidt, B. Meir, K. Elian, D. Ensling, G. Keser, A. Jossen, Measurement of gas pressure inside large-format prismatic lithium-ion cells during operation and cycle aging, *J. Power Sources* 478 (2020) 228661, <http://dx.doi.org/10.1016/j.jpowsour.2020.228661>.
- [16] I. Zilberman, S. Ludwig, M. Schiller, A. Jossen, Online aging determination in lithium-ion battery module with forced temperature gradient, *J. Energy Storage* 28 (2020) 101170, <http://dx.doi.org/10.1016/j.est.2019.101170>.
- [17] X. Feng, C. Weng, X. He, X. Han, L. Lu, D. Ren, M. Ouyang, Online state-of-health estimation for Li-Ion battery using partial charging segment based on support vector machine, *IEEE Trans. Veh. Technol.* 68 (9) (2019) 8583–8592, <http://dx.doi.org/10.1109/TVT.2019.2927120>.
- [18] J. Tian, R. Xiong, W. Shen, F. Sun, Electrode ageing estimation and open circuit voltage reconstruction for lithium ion batteries, *Energy Storage Mater.* 37 (2021) 283–295, <http://dx.doi.org/10.1016/j.ensm.2021.02.018>.
- [19] Q. Zhang, X. Li, C. Zhou, Y. Zou, Z. Du, M. Sun, Y. Ouyang, D. Yang, Q. Liao, State-of-health estimation of batteries in an energy storage system based on the actual operating parameters, *J. Power Sources* 506 (2021) 230162, <http://dx.doi.org/10.1016/j.jpowsour.2021.230162>.
- [20] S. Jenu, A. Hentunen, J. Haavisto, M. Pihlatie, State of health estimation of cycle aged large format lithium-ion cells based on partial charging, *J. Energy Storage* 46 (2022) 103855, <http://dx.doi.org/10.1016/j.est.2021.103855>.
- [21] B. Jiang, H. Dai, X. Wei, Incremental capacity analysis based adaptive capacity estimation for lithium-ion battery considering charging condition, *Appl. Energy* 269 (2020) 115074, <http://dx.doi.org/10.1016/j.apenergy.2020.115074>.
- [22] A. Nuhic, T. Terzimehic, T. Soczka-Guth, M. Buchholz, K. Dietmayer, Health diagnosis and remaining useful life prognostics of lithium-ion batteries using data-driven methods, *J. Power Sources* 239 (2013) 680–688, <http://dx.doi.org/10.1016/j.jpowsour.2012.11.146>.
- [23] N. Omar, M.A. Monem, Y. Firouz, J. Salminen, J. Smekens, O. Hegazy, H. Gaulous, G. Mulder, P. van den Bossche, T. Coosemans, J. van Mierlo, Lithium iron phosphate based battery – Assessment of the aging parameters and development of cycle life model, *Appl. Energy* 113 (2014) 1575–1585, <http://dx.doi.org/10.1016/j.apenergy.2013.09.003>.
- [24] M. Dubarry, C. Truchot, B.Y. Liaw, Synthesize battery degradation modes via a diagnostic and prognostic model, *J. Power Sources* 219 (2012) 204–216, <http://dx.doi.org/10.1016/j.jpowsour.2012.07.016>.
- [25] C. Campestrini, S. Kosch, A. Jossen, Influence of change in open circuit voltage on the state of charge estimation with an extended Kalman filter, *J. Energy Storage* 12 (2017) 149–156, <http://dx.doi.org/10.1016/j.est.2017.04.011>.
- [26] K. Kleiner, P. Jakes, S. Scharner, V. Liebau, H. Ehrenberg, Changes of the balancing between anode and cathode due to fatigue in commercial lithium-ion cells, *J. Power Sources* 317 (2016) 25–34, <http://dx.doi.org/10.1016/j.jpowsour.2016.03.049>.
- [27] C.R. Birk, M.R. Roberts, E. McTurk, P.G. Bruce, D.A. Howey, Degradation diagnostics for lithium ion cells, *J. Power Sources* 341 (2017) 373–386, <http://dx.doi.org/10.1016/j.jpowsour.2016.12.011>.
- [28] C.R. Birk, E. McTurk, S. Zekoll, F.H. Richter, M.R. Roberts, P.G. Bruce, D.A. Howey, Degradation diagnostics for commercial lithium-ion cells tested at -10 °C, *J. Electrochem. Soc.* 164 (12) (2017) A2644–A2653, <http://dx.doi.org/10.1149/2.1401712jes>.
- [29] Y. Gao, J. Jiang, C. Zhang, W. Zhang, Y. Jiang, Aging mechanisms under different state-of-charge ranges and the multi-indicators system of state-of-health for lithium-ion battery with Li(NiMnCo)O₂ cathode, *J. Power Sources* 400 (2018) 641–651, <http://dx.doi.org/10.1016/j.jpowsour.2018.07.018>.
- [30] J.P. Fath, D. Dragicevic, L. Bittel, A. Nuhic, J. Sieg, S. Hahn, L. Alsheimer, B. Spier, T. Wetzel, Quantification of aging mechanisms and inhomogeneity in cycled lithium-ion cells by differential voltage analysis, *J. Energy Storage* 25 (2019) 100813, <http://dx.doi.org/10.1016/j.est.2019.100813>.
- [31] Y. Gao, S. Yang, J. Jiang, C. Zhang, W. Zhang, X. Zhou, The mechanism and characterization of accelerated capacity deterioration for lithium-ion battery with Li(NiMnCo)O₂ cathode, *J. Electrochem. Soc.* 166 (8) (2019) A1623–A1635, <http://dx.doi.org/10.1149/2.1001908jes>.
- [32] X. Jia, C. Zhang, Y. Le Wang, L. Zhang, W. Zhang, The degradation characteristics and mechanism of Li[Ni 0.5 Co 0.2 Mn 0.3]O₂ batteries at different temperatures and discharge current rates, *J. Electrochem. Soc.* 167 (2) (2020) 020503, <http://dx.doi.org/10.1149/1945-7111/ab61e9>.
- [33] J. Schmitt, M. Schindler, A. Oberbauer, A. Jossen, Determination of degradation modes of lithium-ion batteries considering aging-induced changes in the half-cell open-circuit potential curve of silicon-graphite, *J. Power Sources* 532 (9) (2022) 231296, <http://dx.doi.org/10.1016/j.jpowsour.2022.231296>.
- [34] D. Lu, M. Scott Trimboli, G. Fan, R. Zhang, G.L. Plett, Implementation of a physics-based model for half-cell open-circuit potential and full-cell open-circuit voltage estimates: Part II. Processing full-cell data, *J. Electrochem. Soc.* 168 (7) (2021) 070533, <http://dx.doi.org/10.1149/1945-7111/ac11a5>.
- [35] K. Mergo Mbeya, N. Damay, G. Friedrich, C. Forgez, M. Juston, Off-line method to determine the electrode balancing of Li-ion batteries, *Math. Comput. Simul.* 183 (10) (2021) 34–47, <http://dx.doi.org/10.1016/j.matcom.2020.02.013>.
- [36] M. Dubarry, D. Beck, Perspective on mechanistic modeling of Li-Ion batteries, *Account. Mater. Res.* 1 (5) (2022) 242, <http://dx.doi.org/10.1021/accountsmr.2c00082>.
- [37] S. Yang, C. Zhang, J. Jiang, W. Zhang, Y. Gao, L. Zhang, A voltage reconstruction model based on partial charging curve for state-of-health estimation of lithium-ion batteries, *J. Energy Storage* 35 (2021) 102271, <http://dx.doi.org/10.1016/j.est.2021.102271>.
- [38] J. Chen, M.N. Marlow, Q. Jiang, B. Wu, Peak-tracking method to quantify degradation modes in lithium-ion batteries via differential voltage and incremental capacity, *J. Energy Storage* 45 (2022) 103669, <http://dx.doi.org/10.1016/j.est.2021.103669>.
- [39] C. Qian, B. Xu, L. Chang, B. Sun, Q. Feng, D. Yang, Y. Ren, Z. Wang, Convolutional neural network based capacity estimation using random segments of the charging curves for lithium-ion batteries, *Energy* 227 (6058) (2021) 120333, <http://dx.doi.org/10.1016/j.energy.2021.120333>.
- [40] M. Maures, A. Capitaine, J.-Y. Delétage, J.-M. Vinassa, O. Briat, Lithium-ion battery SoH estimation based on incremental capacity peak tracking at several current levels for online application, *Microelectron. Reliab.* 114 (23) (2020) 113798, <http://dx.doi.org/10.1016/j.microrel.2020.113798>.
- [41] V. Pop, H.J. Bergveld, P.P.L. Regtien, J.H.G. Op het Veld, D. Danilov, P.H.L. Notten, Battery aging and its influence on the electromotive force, *J. Electrochem. Soc.* 154 (8) (2007) A744, <http://dx.doi.org/10.1149/1.2742296>.
- [42] H. Popp, N. Zhang, M. Jahn, M. Arrinda, S. Ritz, M. Faber, D.U. Sauer, P. Azais, I. Cendoya, Ante-mortem analysis, electrical, thermal, and ageing testing of state-of-the-art cylindrical lithium-ion cells, e & i, *Elektrotech. Inf. tech.* 137 (4–5) (2020) 169–176, <http://dx.doi.org/10.1007/s00502-020-00814-9>.
- [43] T.M.M. Heenan, A. Jnawali, M.D.R. Kok, T.G. Tranter, C. Tan, A. Dimitrijevic, R. Jervis, D.J.L. Brett, P.R. Shearing, An advanced microstructural and electrochemical datasheet on 18650 Li-Ion batteries with nickel-rich NMC811 cathodes and graphite-silicon anodes, *J. Electrochem. Soc.* 167 (14) (2020) 140530, <http://dx.doi.org/10.1149/1945-7111/abc4c1>.
- [44] J. Sturm, A. Rheinfeld, I. Zilberman, F.B. Spangler, S. Kosch, F. Frie, A. Jossen, Modeling and simulation of inhomogeneities in a 18650 nickel-rich, silicon-graphite lithium-ion cell during fast charging, *J. Power Sources* 412 (2019) 204–223, <http://dx.doi.org/10.1016/j.jpowsour.2018.11.043>.
- [45] X. Li, A.M. Colclasure, D.P. Finegan, D. Ren, Y. Shi, X. Feng, L. Cao, Y. Yang, K. Smith, Degradation mechanisms of high capacity 18650 cells containing Si-graphite anode and nickel-rich NMC cathode, *Electrochim. Acta* 297 (2019) 1109–1120, <http://dx.doi.org/10.1016/j.electacta.2018.11.194>.
- [46] J. Schmitt, M. Rehm, A. Karger, A. Jossen, Aging data, charging curves and battery electric vehicle application profiles of a nickel-rich NMC / silicon-graphite high-energy lithium-ion cell, 2022, <http://dx.doi.org/10.14459/2022mp1690455>, URL <https://mediatum.ub.tum.de/1690455>.

- [47] E. Kirchner, Leistungsübertragung in Fahrzeuggetrieben: Grundlagen der Auslegung, Entwicklung und Validierung von Fahrzeuggetrieben und deren Komponenten, VDI-Buch, Springer Berlin Heidelberg, Berlin, Heidelberg, 2007.
- [48] J. Schmitt, M. Schindler, A. Jossen, Change in the half-cell open-circuit potential curves of silicon-graphite and nickel-rich lithium nickel manganese cobalt oxide during cycle aging, *J. Power Sources* 506 (1) (2021) 230240, <http://dx.doi.org/10.1016/j.jpowsour.2021.230240>.
- [49] S. Ludwig, I. Zilberman, A. Oberbauer, M. Rogge, M. Fischer, M. Rehm, A. Jossen, Adaptive method for sensorless temperature estimation over the lifetime of lithium-ion batteries, *J. Power Sources* 521 (2022) 230864, <http://dx.doi.org/10.1016/j.jpowsour.2021.230864>.
- [50] M. Schindler, J. Sturm, S. Ludwig, A. Durdel, A. Jossen, Comprehensive analysis of the aging behavior of nickel-rich, silicon-graphite lithium-ion cells subject to varying temperature and charging profiles, *J. Electrochem. Soc.* (2021) <http://dx.doi.org/10.1149/1945-7111/ac03f6>.
- [51] I. Zilberman, J. Sturm, A. Jossen, Reversible self-discharge and calendar aging of 18650 nickel-rich, silicon-graphite lithium-ion cells, *J. Power Sources* 425 (2019) 217–226, <http://dx.doi.org/10.1016/j.jpowsour.2019.03.109>.
- [52] E. Coron, S. Geniès, M. Cugnet, P.X. Thivel, High-energy Li-Ion cells: Impact of electrode ageing on second life viability, *J. Electrochem. Soc.* 168 (10) (2021) 100539, <http://dx.doi.org/10.1149/1945-7111/ac3112>.
- [53] S. Schweidler, L. de Biasi, A. Schiele, P. Hartmann, T. Brezesinski, J. Janek, Volume changes of graphite anodes revisited: A combined operando X-ray diffraction and in situ pressure analysis study, *J. Phys. Chem. C* 122 (16) (2018) 8829–8835, <http://dx.doi.org/10.1021/acs.jpcc.8b01873>.
- [54] R. Jung, M. Metzger, F. Maglia, C. Stinner, H.A. Gasteiger, Oxygen release and its effect on the cycling stability of $\text{LiNi}_x\text{Mn}_y\text{Co}_z\text{O}_2$ (NMC) cathode materials for Li-Ion batteries, *J. Electrochem. Soc.* 164 (7) (2017) A1361–A1377, <http://dx.doi.org/10.1149/2.0021707jes>.
- [55] I. Zilberman, J. Schmitt, S. Ludwig, M. Naumann, A. Jossen, Simulation of voltage imbalance in large lithium-ion battery packs influenced by cell-to-cell variations and balancing systems, *J. Energy Storage* 32 (2020) 101828, <http://dx.doi.org/10.1016/j.est.2020.101828>.
- [56] S. Schindler, G. Baure, M.A. Danzer, M. Dubarry, Kinetics accommodation in Li-ion mechanistic modeling, *J. Power Sources* 440 (23) (2019) 227117, <http://dx.doi.org/10.1016/j.jpowsour.2019.227117>.
- [57] C. Campestrini, M.F. Horsche, I. Zilberman, T. Heil, T. Zimmermann, A. Jossen, Validation and benchmark methods for battery management system functionalities: State of charge estimation algorithms, *J. Energy Storage* 7 (2016) 38–51, <http://dx.doi.org/10.1016/j.est.2016.05.007>.